Top Curr Chem (2014) 347: 47–98
DOI: 10.1007/128_2013_503

Published online: 2 February 2014

Status in Calculating Electronic Excited States in Transition Metal Oxides from First Principles

Leah Isseroff Bendavid and Emily Ann Carter

Abstract Characterization of excitations in transition metal oxides is a crucial step in the development of these materials for photonic and optoelectronic applications. However, many transition metal oxides are considered to be strongly correlated materials, and their complex electronic structure is challenging to model with many established quantum mechanical techniques. We review state-of-the-art first-principles methods to calculate charged and neutral excited states in extended materials, and discuss their application to transition metal oxides. We briefly discuss developments in density functional theory (DFT) to calculate fundamental band gaps, and introduce time-dependent DFT, which can model neutral excitations. Charged excitations can be described within the framework of many-body perturbation theory based on Green's functions techniques, which predominantly employs the *GW* approximation to the self-energy to facilitate a feasible solution to the quasiparticle equations. We review the various implementations of the *GW* approximation and evaluate each approach in its calculation of fundamental band gaps of many transition metal oxides. We also briefly review the related Bethe–Salpeter equation (BSE), which introduces an electron–hole interaction between *GW*-derived quasiparticles to describe accurately neutral excitations. Embedded correlated wavefunction theory is another framework used to model localized neutral or charged excitations in extended materials. Here, the electronic structure of a small cluster is modeled within correlated wavefunction theory, while its coupling to its environment is represented by an embedding potential. We review a number of techniques to represent this background potential, including electrostatic representations and electron density-based methods, and evaluate their application to transition metal oxides.

Keywords Correlated wavefunction theory · Density functional theory · Embedding potential · Excited states · *GW* approximation · Transition metal oxides

L.I. Bendavid and E.A. Carter (✉)
Princeton University, Princeton, NJ, USA
e-mail: eac@princeton.edu

Contents

1 Introduction

Transition metal oxides are an emerging class of materials for use in a wide variety of photonic and optoelectronic applications, such as light-energy conversion through photovoltaics or photocatalysis, light emitting diodes, and transparent conducting oxides. The electronic band structure and optical absorption properties of these materials are fundamental to evaluating their functionality in these applications. Characterization of their ground and excited states will help to improve their performance in these technologies, particularly for solar energy conversion applications, where the lifetime of the optically excited state is a crucial factor that dictates device efficiency.

The response of a material to light absorption can typically be described by either charged excitations or neutral excitations (Fig. 1). Charged excitations occur in photoemission (PE) and inverse photoemission (IPE) processes. In PE, a material absorbs an energetic photon with an energy $h\nu$ to excite an electron in an occupied valence state and emit it in the vacuum continuum. Irradiation can be with ultraviolet light in ultraviolet PE spectroscopy (UPS) or X-rays in X-ray PE spectroscopy (XPS). In IPE, the material absorbs an electron with a kinetic energy E_K into an unoccupied state and emits a photon with an energy $h\nu'$. PE spectra (PES) therefore correspond to the distribution of occupied states, while IPE spectra (IPES) correspond to the distribution of unoccupied states. The fundamental gap, E_g, is defined as the difference between the lowest ionization potential (IP) from PE and the highest electron affinity (EA) from IPE. Neutral excitations are those that occur during optical absorption,

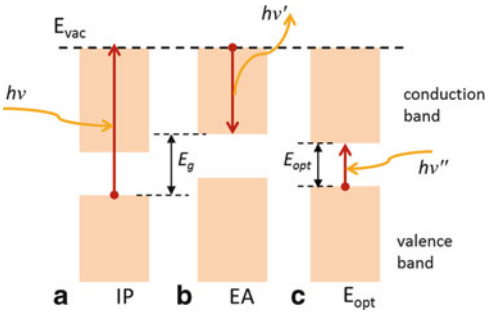

Fig. 1 A representation of the band structure, showing the charged excitations occurring in (*a*) the lowest IP in PE and (*b*) the highest EA from IPE, the difference of which is the fundamental gap, E_g = IP−EA. The lowest neutral excitation is shown in (*c*), whose excitation energy is defined as the optical band gap, E_{opt}. The difference between E_{opt} and E_g is the exciton binding energy. The band edge positions represent the final state energies after the excitation

when a photon with an energy $h\nu''$ is absorbed to excite an electron from the valence band to the conduction band. The optical gap, E_{opt}, is defined as the energetic difference between the lowest excited state and the isoelectronic ground state, where the transition between the two must be dipole-allowed. E_g and E_{opt} are not equivalent due to the interaction energy between the excited electron and the hole it leaves behind (the "exciton") in a neutral excitation. The difference between the two (E_g−E_{opt}) therefore corresponds to the exciton binding energy.

Computing the PES, IPES, optical absorption spectra, fundamental band gap, and optical gap is an integral part of the design and understanding of transition metal oxides for optical and optoelectronic applications. Electronic structure theory offers a number of theoretical approaches to calculate these properties. These methods can largely be classified into two subdivisions: those that are rooted in Green's function methods and those that employ a multi-determinant many- electron wavefunction. No single theory is appropriate for calculating all of the aforementioned observables [1]. Computing these properties from first principles is even more challenging for transition metal oxides than for main group compounds, as many of these materials are considered to be strongly correlated. Consequently, these theoretical methods have varying levels of success for these applications. In this chapter we discuss some of the most powerful methods in quantum mechanics that are used to calculate optical and PE observables, and we review their application to transition metal oxides.

In Sect. 2 we begin with a brief discussion of density functional theory (DFT), which is the workhorse of quantum mechanics for ground-state properties of materials. Because DFT is a ground-state theory, it cannot be used to predict many of the excited state properties of interest. However, variations of DFT have been proposed that may be appropriate for the prediction of the fundamental gap and PES. Although DFT is not the main focus of this chapter, it serves as a starting point for many higher levels of theory, which warrants its introduction. To close this section we briefly review time-dependent DFT (TD-DFT) and its application to predicting neutral excitations in transition metal oxides.

In Sect. 3 we continue with a discussion of the *GW* approximation, which explicitly describes charged excitations using a quasiparticle (QP) formalism. The *GW* approximation can therefore be used to calculate PES, IPES, and the fundamental gap. We discuss the various forms of *GW*, each of which approaches its implementation in a different manner. At the end of this section, we introduce the Bethe–Salpeter equations, which incorporate the electron–hole interactions needed to model neutral excitations and calculate optical absorption spectra. For all of the methods discussed we cite examples of their application to transition metal oxides, where available.

In Sect. 4 we discuss the techniques that rely on multi-determinant wavefunctions, known as correlated wavefunction methods. We introduce correlated wavefunction theory, discussing the various levels of theory used to model ground and excited states of materials. We describe their application to extended materials through the use of the embedded cluster model, where a small cluster is described within correlated wavefunction theory, and the coupling of the environment to the cluster is accounted for with an embedding potential. We review the representation of the embedding potential using an electrostatic model of the background, as well as techniques that use the electron density to derive a DFT-based or numerical embedding potential. Here, too, we discuss cases where these methods have been applied to transition metal oxides.

Finally, we close the chapter in Sect. 5 with some concluding remarks.

2 Density Functional Theory

2.1 Kohn–Sham Density Functional Theory

The fundamental principle of DFT was established by Hohenberg and Kohn [2], who proved that the ground state properties of any non-degenerate system of electrons can be uniquely determined by its electron density. Specifically, they derived a functional of the electron density whose minimum corresponds to the ground state energy. While their theory is formally exact, the approach remained intractable because of the unknown form of the energy functional. DFT became a practical tool with the scheme presented by Kohn and Sham [3], where the physical problem of interacting electrons moving in an external potential is mapped onto a fictitious set of non-interacting electrons subject to a common effective potential. The Kohn-Sham (KS) reference wavefunction is represented as a single Slater determinant constructed from one-electron orbitals representing the spatial distribution of these non-interacting electrons, and the interacting electron density is in fact given by the sum of the densities of the occupied KS orbitals:

$$\rho(\mathbf{r}) = \sum_{n,\,\mathrm{occ}} |\psi_n(\mathbf{r})|^2. \tag{1}$$

The energy functional in KS-DFT is

$$E[\rho] = T_s[\rho] + \int V_{ext}(\mathbf{r})\rho(\mathbf{r})d\mathbf{r} + J[\rho] + E_{xc}[\rho], \tag{2}$$

where T_s is the non-interacting electron kinetic energy, which within KS-DFT is expressed as a functional of the occupied non-interacting one-electron orbitals:

$$T_s[\{\psi_i\}] = -\frac{1}{2}\sum_{n}^{occ}\langle\psi_n|\nabla^2|\psi_n\rangle. \tag{3}$$

The second term is the electrostatic interaction of the electron density with an external potential V_{ext}, such as the electron-ion potential. J is the classical Hartree repulsion energy,

$$J[\rho] = \frac{1}{2}\int\frac{\rho(\mathbf{r})\rho(\mathbf{r}')}{|\mathbf{r}-\mathbf{r}'|}d\mathbf{r}d\mathbf{r}', \tag{4}$$

and E_{xc} is the exchange-correlation energy, which accounts for all non-classical electron–electron interactions, as well as the difference between the interacting and non-interacting electron kinetic energy.

The KS orbitals, $\psi_i(\mathbf{r})$, and their energies, ϵ_i, are obtained as the eigenfunctions and eigenvalues in the self-consistent solution of the KS equations

$$\left(-\frac{\nabla^2}{2} + V_{ext}(\mathbf{r}) + V_H([\rho];\mathbf{r}) + V_{xc}([\rho];\mathbf{r})\right)\psi_i(\mathbf{r}) = \epsilon_i\psi_i(\mathbf{r}), \tag{5}$$

where V_{ext} is the electron-ion potential, V_H is the Hartree potential, and V_{xc} is the exchange-correlation potential.

The KS formalism for DFT is exact, and would reproduce the physical electron density if the functional form of the exchange-correlation potential were known exactly. However, only approximate forms of this potential are known. The search for an accurate exchange-correlation functional is one of the greatest challenges in DFT. KS-DFT can be used to model systems with several hundred atoms, as it scales as O(N^3) with respect to system size, although lower scaling methods have been designed [4]. In periodic KS-DFT, the calculational expense also scales linearly with respect to the number of k-points that sample the Brillouin zone.

2.2 *Exchange-Correlation Functionals, DFT+U, and Hybrid DFT*

The simplest approximation for exchange and correlation is the local density approximation (LDA), where the exchange-correlation energy at each point in

space is approximated as that of a homogeneous electron gas with the same density. The exact exchange-correlation energy for a homogeneous electron gas was calculated by Ceperley and Alder using quantum Monte Carlo simulations [5], and there are a number of functional forms using this data [6–8]. The LDA works quite well for materials with nearly homogeneous electron densities, but is typically inaccurate when there are large fluctuations of the density. The generalized gradient approximation (GGA) improves upon the LDA formulation by expressing the exchange-correlation energy as a functional of both the local density and the gradient of the density, to provide a better description of systems with fluctuating densities. A number of GGA functionals have been developed [9–14], including the widely used Perdew–Burke–Ernzerhof (PBE) functional [10, 11]. The LDA tends to underestimate bond lengths and lattice constants and overestimate bond energies, while the GGA exhibits the opposite tendencies. The eigenvalue gaps of both methods significantly underestimate the band gap.

The underestimation of the band gap with local and semilocal exchange-correlation functionals is largely due to the self-interaction error, which is due to the inexact cancellation of self-interaction that arises in the mean field formulation of the Hartree energy. This interaction is cancelled exactly by the exchange component in Hartree–Fock (HF) theory, but fails to be fully cancelled by the inexact exchange-correlation functionals in KS-DFT. The spurious, repulsive self-interaction produces excess electron delocalization upon variational optimization, which is especially significant in systems with highly localized electrons such as the *d*-electrons in first row, late transition metal oxides.

The self-interaction error can be corrected by reintroducing some form of exact exchange into the exchange-correlation functional. The DFT+U method [15–22] reduces the self-interaction error by introducing an approximation to intra-atomic exact exchange. Specifically, it applies a parameterized Hartree–Fock-like potential to the highly localized electrons on an atom. This potential is controlled by U and J parameters, which are chosen to mimic the effective Coulomb (U) and exchange (J) on-site (intra-atomic) interactions between electrons. In practical DFT calculations, such as formulated by Dudarev et al. [21, 22], it is actually the difference between U and J that is the effective parameter, and U and J are often combined by re-defining $U_{\text{eff}} = U - J$. The DFT+U approximation to exact exchange involves only a minimal increase in computational effort above the standard DFT method.

The values of U and J – or more specifically, the quantity $U{-}J$ – strongly influence electron localization and the band gap of a material, so it is important that U and J values are chosen to accurately represent the effective on-site interactions. One approach is to choose the $U{-}J$ that best reproduces empirical data. To be free from empiricism, other procedures rely on first principles methods such as constrained LDA [23–25] or a constrained random phase approximation (RPA) [26–29], which extract U and J from a calculation where the electron occupation is held fixed on a specific site. However, these techniques may still suffer from the shortcomings of the approximate exchange-correlation potential used in DFT. To

remove the dependence on a potentially inaccurate functional, one can calculate $U-J$ self-consistently using DFT+U within a linear-response approach [30–32], or one can derive U and J using constrained RPA within a self-consistent DFT+U calculation [33]. Alternatively, the ab initio method developed by Mosey and Carter [34, 35] derives U and J from unrestricted Hartree-Fock (UHF) theory, which is free from the self-interaction error of DFT with approximate exchange-correlation potentials. Finally, the procedure proposed by Kioupakis et al. [36] chooses $U-J$ to minimize a subsequent single perturbative GW correction. This approach is founded on the principle that the mean field theory must be close to the final GW result for the perturbation theory to be operative. Their ideal value for $U-J$ is thus at the point where the DFT+U and GW band gap curves cross, which also pinpoints the predicted band gap value.

Exact exchange can be more explicitly accounted for in the DFT reference by using exact exchange within an optimized effective potential (denoted OEPx or OEPx(cLDA) when LDA correlation is added); here a local potential is used to approximate the non-local Fock operator [37]. This enables complete elimination of the self-interaction error while maintaining a local KS potential. The main challenges with OEP methods are their expense and numerical complexity [38–49].

Alternatively, hybrid functionals can offer a better description of electron–electron interactions by introducing a nonlocal exact exchange potential that is mixed in with DFT approximate exchange and applied to all electrons in the system. DFT exchange tends to underestimate ionicity and the band gap, so adding in HF exchange, which alone overestimates those same quantities balances these tendencies. The hybrid functional scheme was first proposed by Becke [50]. There are a number of hybrid functionals, all of which incorporate a portion of a nonlocal exact exchange potential into the local KS potential. The PBE0 [51] functional is a hybrid functional which replaces one quarter of PBE exchange with HF exchange, leaving correlation to be treated solely by the PBE functional. The mixing parameter of 1/4 is justified by perturbation theory considerations [52]. For an added degree of flexibility within the functional form, range-separated hybrid functionals introduce a range-separating parameter, which further divides the treatment of exchange as a function of interaction distance. Range-separation was first proposed by Savin and coworkers [53–55], but many range-separated hybrid functionals now exist [56–61]. The Heyd–Scuseria–Ernzerhof (HSE) [62–65] functional builds upon the PBE0 functional by introducing such a range-separation parameter, further dividing exchange such that only the short range component introduces HF exchange. The contribution of HF exchange therefore decreases in HSE with respect to PBE0, but is still greater than DFT+U. Accordingly, the eigenvalue gaps of HSE tend to fall between the two other theories, with the largest gaps predicted by PBE0. There is also the popular B3LYP functional, which mixes LDA exchange-correlation with HF exchange and GGA exchange and correlation [6, 66–68]. In B3LYP, the three mixing parameters were determined by fitting to experimental atomization energies.

2.3 Fundamental Band Gap from DFT

The single particle eigenvalues in standard KS-DFT with local or semilocal exchange-correlation functionals do not formally correlate with the energies of the states probed in PE and IPE spectroscopy. The only eigenvalue in KS-DFT that has a formal interpretation is the one associated with the highest energy occupied orbital, which is equal to the negative of the lowest IP from PE [69–71]. Although no similar relationship can be derived between the lowest energy unoccupied orbital and the EA, the difference between the highest energy occupied and lowest energy unoccupied orbital eigenvalues is often interpreted as the fundamental band gap. Sham and Schlüter [72] and Perdew and Levy [73] showed that the eigenvalue gap differs from the fundamental band gap by an explicit correction given by the derivative discontinuity of the exchange-correlation energy. This implies that it is not possible to use the standard KS-DFT framework to obtain the fundamental band gap of materials via interpretation of the KS eigenvalues. This is also indicative of a broader disconnect between the KS density of states and the PES/IPES. Although the fundamental band gap is only a part of the larger complex problem of predicting absorption and emission spectra, in fact most work in this area has focused on the smaller goal of adapting KS-DFT to calculate the band gap.

One strategy is to avoid completely a dependence on the KS eigenvalues by calculating IPs and EAs explicitly via electron removal and addition, and to derive the fundamental gap using the well-known ΔSCF method. The Δ-sol method by Chan and Ceder [74] extends the ΔSCF method to solids and derives the band gap from DFT total energy differences of charged periodic unit cells. To prevent divergence of the electrostatic energy of the periodic array, they use the conventional approach of introducing a neutralizing jellium background [75], and treat the image-charge interaction error using the energy correction of Makov and Payne [76]. However, the a posteriori correction to the energy does not correct for the adulteration of the underlying potential by the jellium, and the topology of the local electrostatic potential will be misrepresented in this approach [77, 78]. In the application of the Δ-sol method to ZnO, Chan and Ceder used DFT with the LDA for exchange-correlation to calculate a LDA/Δ-sol band gap of 3.5 eV. This is close to the experimental gap of 3.37 [79], and is a marked improvement over the LDA eigenvalue gap of 0.8 eV.

Another approach to calculate the fundamental gap is to add back in the missing derivative discontinuity as a correction to the KS-DFT eigenvalue gap. Stein et al. [80] introduced a correction term that is derived from the curvature of the exchange-correlation energy as a function of electron number. Approximate exchange-correlation functionals compensate for the missing derivative discontinuity by introducing curvature to the exchange-correlation energy, and so the approach of Stein et al. uses this curvature to derive the missing derivative discontinuity. The missing derivative discontinuity is then added as a correction to the eigenvalue gap, in accordance with the derivations of Sham and Schlüter [72] and Perdew and Levy [73]. Thus far, this approach has only been applied to molecules.

Calculation of the fundamental gap and formal interpretation of the DFT eigenvalues may be possible within an alternative DFT scheme. While KS-DFT maps the density to a single Slater determinant of non-interacting orbitals, other mapping schemes are possible. Within the generalized KS scheme, the density is mapped to an interacting model system that partially accounts for electron–electron interaction, whose potential is no longer strictly local. This nonlocal potential can incorporate the derivative discontinuity into the band gap, leading to a formal relationship between the lowest energy unoccupied orbital and the EA, with which a fundamental band gap can be derived [81, 82].

An example of a generalized KS scheme that employs nonlocal functionals is one that uses hybrid functionals (as discussed in the previous section), where range-separated hybrid functionals contain an added degree of flexibility via the range-separation parameter. Range-separated hybrid functionals optimize the range separation parameter in different ways, and typically the range separation parameter is optimized as a universal parameter. However, this parameter can be shown to be a functional of the density [83], and differing values are needed at varying densities of the homogeneous electron gas [84]. This indicates that the range separation parameter unfortunately should be treated as a system-dependent parameter that is optimized on a material-specific basis.

One range-separated hybrid functional that treats the range separation parameter as system-dependent is the Baer–Neuhauser–Livshits (BNL) functional [83, 84], which tunes the range separation parameter by actively enforcing the DFT-Koopmans' theorem [85]. This approach has been used successfully in determining the parameters for a range of molecules to obtain their fundamental gaps [86], and has also been shown to be a good method for producing the QP spectra of molecules [87]. However, the tuning procedure can only be applied to molecules, and a robust tuning method needs to be developed for solids for this approach to be appropriate for extended materials [88]. Consequently, while the BNL functional and other generalized KS schemes have the potential to be inexpensive and robust methods to determine the fundamental band gap for transition metal oxides, they remain largely out of reach at present. It is therefore necessary to turn to higher levels of theory that are designed to model charged excitations explicitly, such as many-body perturbation theory, of which *GW* is one of the most prominent approximations. However, before elaborating on *GW* theory, we first consider TD-DFT, which can be used to describe neutral excitations.

2.4 Time-Dependent Density Functional Theory

The neutral excitation spectrum and optical gap can be calculated within the framework of linear-response TD-DFT [89–97], which describes the evolution of the electron density in response to a time-dependent external potential. Neutral excitation energies can be obtained as the poles of the exact linear response function. Using the formalism of TD-DFT, Petersilka et al. [90] related the exact

response function χ to the KS non-interacting response function χ_{KS}, where the Dyson-type equation is dependent on the nonlocal, energy-dependent exchange correlation kernel f_{XC} (the functional derivative of the exchange-correlation potential with respect to the density):

$$\chi\left(\mathbf{r},\mathbf{r}',\omega\right) = \chi_{\mathrm{KS}}\left(\mathbf{r},\mathbf{r}',\omega\right) + \int \mathrm{d}^3x \int \mathrm{d}^3x' \chi_{KS}\left(\mathbf{r},\mathbf{x},\omega\right)\left(\frac{1}{|\mathbf{x}-\mathbf{x}'|} + f_{\mathrm{XC}}\left(\mathbf{x},\mathbf{x}',\omega\right)\right)\chi\left(\mathbf{x}',\mathbf{r}',\omega\right). \tag{6}$$

The non-interacting response function can be derived directly from the solution to the static KS equations. This approach is formally exact, but its accuracy is limited by the approximations for the static exchange-correlation potential and the frequency-dependent exchange-correlation kernel, which are typically modeled by local functionals and the adiabatic approximation. The application of TD-DFT to extended systems is challenging, largely because the typically local approximation to the exchange-correlation functional used in the TD-DFT kernel does not capture the important long-range interactions in extended materials [95, 98, 99]. There have also been practical difficulties applying TD-DFT to simulate the optical spectra of larger systems. The Liouville-Lanczos approach implemented by Baroni and coworkers [100, 101] addresses this difficulty and enables the fast and efficient computation of the full spectrum of complex periodic systems. TD-DFT scales formally as $O(N^3)$, and therefore represents a powerful means of modeling optical excitations with a computational expense not much greater than KS-DFT.

Thus far, TD-DFT has performed quite well in calculating optical excitations in transition metal oxides, although many calculations employ cluster models to avoid the challenge in describing long-range interactions. Many applications of TD-DFT to transition metal oxides employ hybrid exchange-correlation functionals, which improve the description of longer range interactions. Others use a DFT+U functional to correct for the failure of the local approximation to exchange-correlation. (We have not found applications of TD-DFT to transition metal oxides that employ local or semilocal functionals.) One application has been to determine the optical properties of ZnO nanoparticles. De Angelis and Armelao [102] calculated the lowest optical transition energies of finite 1D, 2D, and 3D ZnO nanostructures using TD-DFT with the B3LYP functional. They found a lowest excitation energy of 3.59 eV for the ZnO nanoparticle (a $(ZnO)_{111}$ cluster with a diameter ~0.13 nm), in comparison to the experimental gap of 4.0 eV observed for particles with a diameter below 0.5 nm [103]. Malloci et al. [104] used TD-DFT with the BP86 functional to correlate ZnO nanoparticle size and structure with its optoelectronic properties. They found that the optical gap and exciton binding energy decrease with increasing particle size, as is expected due to decreasing quantum confinement. TD-DFT has been similarly applied to TiO_2 nanostructures. De Angelis et al. [105] used TD-DFT with the B3LYP functional to study the lowest excited states of anatase $(TiO_2)_{38}$ nanoparticles,

predicting excitation energies of 3.12–3.20 eV. Suzuki et al. [106] used TD-DFT with long-range corrected Becke exchange [107] to study the effect of oxygen vacancies on excitation energies in anatase TiO_2 nanoparticles. They found that oxygen defects cause strong absorption peaks at 1.5, 1.9, and 2.8 eV, which are consistent with the coloration of TiO_2 crystals reduced by activated carbon [108, 109]. Govind et al. [110] used TD-DFT with the B3LYP functional to calculate the optical absorption spectrum of bulk rutile, modeled as a large rutile TiO_2 cluster terminated by pseudo-hydrogen saturators. They predicted an absorption edge of ~3.0 eV consistent with experiment (~2.9 eV [111, 112]), and found that N-doping lowered the absorption edge by ~0.9 eV, in comparison to the experimental decrease of about ~0.7 eV. TD-DFT has also been used in bulk calculations of NiO. Lee et al. [113] derived the dynamical linear response of the LDA+*U* functional within the TD-DFT framework on a basis of Wannier functions, and applied it to study the bound *d*–*d* Frenkel excitons in NiO, predicting exciton excitation energies at 1–2 eV in comparison to 0.6–3.5 eV from experiment [114, 115]. Finally, Sottile et al. [94] showed how the inclusion of local field effects in the response function is crucial in describing higher energy excitations from the semicore states in electron energy loss spectra for bulk ZrO_2 and TiO_2. These applications show that TD-DFT is a very promising method for calculating neutral excitations in transition metal oxides; next we turn to many-body perturbation theory to describe charged excitations that TD-DFT cannot.

3 *GW* Approximation

3.1 *Fundamental Theory of the* GW *Approximation*

The single particle excitations that occur in PE and IPE spectroscopy and that define the fundamental gap can be described in terms of electron and hole QPs, where a QP is comprised of a bare particle and its surrounding screening charge cloud. The qualitative QP picture can be formally represented by many-body perturbation theory. Specifically, the electron and hole QP energies, ϵ_n, and wavefunctions, ψ_n, can be obtained via solution of the QP equation [116]

$$\left(\hat{T} + V_{\text{ext}} + V_{\text{H}}\right)\psi_n(\mathbf{r}) + \int \mathrm{d}\mathbf{r}' \sum \left(\mathbf{r}, \mathbf{r}'; \epsilon_n\right)\psi_n\left(\mathbf{r}'\right) = \epsilon_n \psi_n(\mathbf{r}), \tag{7}$$

which differs from the KS equation of (5) by replacing the exchange-correlation potential with the self-energy, Σ. The self-energy is a nonlocal, non-Hermitian, energy-dependent operator that accounts for all non-classical electron–electron interactions. The QP equation can be solved only with a well-founded definition of the self-energy operator. Such a formalism was defined by Hedin [117], whose set of integro-differential equations relate the self-energy to the Green's function G, the polarizability P, the screened (W) and bare (v) Coulomb interaction, and the

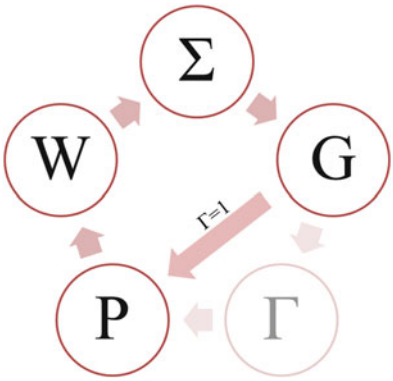

Fig. 2 Hedin's pentagon, illustrating the self-consistent loop of Hedin's equations. Under the *GW* approximation, the loop bypasses the calculation of Γ (shown with some transparency)

vertex function Γ, thus providing a perturbative, self-consistent approach to solving for the self-energy. In the following set of equations we employ a shorthand notation for the space-time coordinates, defining $1 \equiv (\mathbf{r}_1,t_1)$:

$$P(1,2) = -i\int G(1,3)G(4,1)\Gamma(3,4,2)d(3,4), \tag{8}$$

$$W(1,2) = v(1,2) + \int v(1,3)P(3,4)W(4,2)d(3,4), \tag{9}$$

$$\Sigma(1,2) = i\int G(1,3)\Gamma(3,2,4)W(4,1)d(3,4), \tag{10}$$

$$\Gamma(1,2,3) = \delta(1,2)\delta(1,3) + \int \frac{\delta\Sigma(1,2)}{\delta G(4,5)} G(4,6)G(7,5)\Gamma(6,7,3)d(4,5,6,7). \tag{11}$$

The final equation to complete the self-consistent loop (shown in Fig. 2) in Hedin's relationships is Dyson's equation, which links the non-interacting system with Green's function G_0 to the fully interacting one (G) via the self-energy Σ:

$$G(1,2) = G_0(1,2) + \int G_0(1,3)\Sigma(3,4)G(4,2)d(3,4). \tag{12}$$

While theoretically this closed system of equations could be solved self-consistently to obtain Σ, practically, a fully self-consistent procedure is not implementable for even the simplest systems. Hedin proposed the now widely used *GW* approximation, which approximates the vertex function by its zeroth order term [117]:

$$\Gamma(1,2,3) = \delta(1,2)\delta(1,3) \tag{13}$$

The expression for the self-energy within this approximation therefore becomes

$$\Sigma(1,2) = iG(1,2)W(1,2), \tag{14}$$

from which the "*GW* approximation" derives its name.

3.2 GW *as a Single Perturbation:* G_0W_0

The approximation for the vertex function makes it easier to iterate through Hedin's equations to construct self-consistently the self-energy, but even this is still mathematically challenging. A common procedure is to apply the self-energy as perturbative correction within the QP equation, where the self-energy is constructed from the best mean field results available. This approach is denoted G_0W_0, where typically, G_0 and W_0 are calculated using the eigenvalues and eigenfunctions of a Hermitian single-particle reference such as KS-DFT (or some variant). These are used to construct the self-energy according to (14), which is then used in a single iteration of the QP equation applied to the reference eigenfunctions. This procedure is founded on the assumption that the KS equations can be a good approximation to the QP equations, as they differ only in the operator accounting for non-classical electron–electron interactions (the exchange-correlation potential in KS theory vs the self-energy of the QP equation). Within a first order perturbation, the QP wavefunctions are taken to be identical to the KS wavefunctions, and the QP energies ϵ_n can be evaluated as

$$\varepsilon_n = \epsilon_n + Z_n(\epsilon_n)\langle\psi_n|\Sigma(\epsilon_n) - V_{\mathrm{xc}}|\psi_n\rangle, \tag{15}$$

where V_{xc} is the exchange-correlation potential of the reference Hamiltonian, ϵ_n are the KS eigenvalues, and Z_n is a renormalization factor, $Z_n = \left(1/\left(1 - \frac{\partial\Sigma}{\partial\epsilon}\right)\right)$, that accounts for the frequency dependence of Σ.

3.2.1 DFT/G_0W_0

Typically, the reference exchange-correlation potential employed is the LDA [118]. However, the LDA fails for materials with highly localized electrons, such as the *d*- or *f*-electrons in transition metal oxides, due to its inexact correction of electron self-interaction (known as the self-interaction error). The self-interaction error results in LDA wavefunctions that are not localized enough, for which a single perturbative G_0W_0 correction often fails to compensate.

The shortcomings of the LDA/G_0W_0 approach are evident in the treatment of many transition metal oxides, as shown in Table 1. We focus here on the predictive accuracy of G_0W_0 with respect to the band gap, which may be an indicator for its accuracy in the larger goal of predicting the full PES/IPES. LDA and LDA/G_0W_0

Table 1 LDA eigenvalue gaps and LDA/G_0W_0 QP gaps for a number of transition metal oxides in comparison with experimental fundamental gaps (some optical gaps are reported in instances where no fundamental gaps are available, marked with an asterisk in the table footnotes; the same convention is used in all subsequent tables)

	E_g(LDA) (eV)	E_g(LDA/G_0W_0) (eV)	E_g(Exp.) (eV)
TiO_2-rutile	1.75[a]	3.34[a]	3.3 ± 0.5[b]
TiO_2-anatase	2.02[a]	3.56[a]	3.4[c]
VO_2	0[d]	0[d]	0.2–0.7[e]
NiO	0.2[f]	1.0[f], 1.1[g]	4.3[h]
Cu_2O	0.54[i]	1.34[i]	2.17[j]
ZnO	0.71[g]	2.51[g]	3.37[k]
CdO	0[g]	0.10[g]	0.84[l], 1.2[m]
ZrO_2	3.58[n]	4.99[n]	5.5[o]
HfO_2	3.95[n]	5.45[n]	5.7[o]

[a] [135]; [b] [136]; [c] [137]*; [d] [119]; [e] [138]; [f] [120]; [g] [121]; [h] [139]; [i] [134]; [j] [140]*; [k] [79]*; [l] [141]*; [m] [142]*; [n] [143]; [o] [144]

both fail to open a gap (i.e., predict a gap between the valence and conduction bands) for the lower-temperature monoclinic insulating phase of VO_2, predicting metallic character instead [119]. The LDA and LDA/G_0W_0 gaps for NiO also both fall well below the experimental gap [120, 121]. The electronic structure of NiO is inaccurately described, in that the character of the top of the valence band is predicted to be predominantly Ni 3d, which is inconsistent with a widely accepted model of NiO as a charge transfer insulator [122–133]. The band gaps of Cu_2O, ZnO, CdO, ZrO_2, and HfO_2 are similarly underestimated with LDA and LDA/G_0W_0 [121, 134]. The failure of the LDA in ZnO can be attributed to the under-prediction of the metal *d*-electron binding energies, which at these too-low energies will hybridize with the oxygen 2*p*-states at the valence band maximum. This pushes the O 2*p*-states slightly higher and decreases the gap. For TiO_2, LDA/G_0W_0 performs relatively well, as it produces QP spectra for TiO_2 that agree well with PES/IPES and calculates fundamental gaps close to experiment [135].

Replacing the LDA reference with a GGA exchange-correlation functional, specifically the PBE functional, did not improve the prediction of theoretical band gaps for Cu_2O [145] and ZnO [146] (Table 2). PBE/G_0W_0 also predicts an underestimated gap for Fe_2O_3 [147]. The change from LDA/G_0W_0 resulted in slightly larger fundamental gaps predicted with PBE/G_0W_0 for rutile and anatase, worsening agreement with experiment for anatase but not significantly impacting accuracy for rutile [148].

3.2.2 DFT+U/G_0W_0

There are two approaches to remedy the failure of the standard LDA/G_0W_0 approach. The first is to replace the LDA (or GGA) reference with a more accurate reference Hamiltonian that will be closer to the final *GW* solution, thereby

Table 2 PBE eigenvalue gaps and PBE/G_0W_0 QP gaps for a number of transition metal oxides in comparison with experimental fundamental gaps

	E_g(PBE) (eV)	E_g(PBE/G_0W_0) (eV)	E_g(Exp.) (eV)
TiO_2-rutile	1.93[a]	3.59[a]	3.3 ± 0.5[b]
TiO_2-anatase	2.15[a]	3.83[a]	3.4[c]
Fe_2O_3	0.6[d]	1.3[d]	2.6 ± 0.4[e]
Cu_2O	0.43[f]	1.39[f]	2.17[g]
ZnO	0.67[h]	2.12[h]	3.37[i]

[a] [148]; [b] [136]; [c] [137]*; [d] [147]; [e] [149]; [f] [145]; [g] [140]*; [h] [146]; [i] [79]*

minimizing the perturbation. The second approach is to introduce some form of self-consistency so *GW* will be independent of the starting point, thereby reducing the impact of any inaccuracy in the reference Hamiltonian.

Within the first approach, the problem then lies in identifying a more appropriate reference Hamiltonian for the material being studied. As described earlier, the self-interaction error is the main cause of band gap underestimation in local and semilocal exchange-correlation functionals. The DFT+*U* method is one approach to reduce the self-interaction error by introducing an approximation to exact exchange, where the material-specific parameters *U* and *J* can be determined via a number of different methods.

Table 3 shows the QP gaps calculated with a G_0W_0 perturbation on a DFT+*U* reference Hamiltonian. These studies determined $U-J$ values using a number of the approaches described in Sect. 2.2. Isseroff and Carter [145] chose a $U-J$ for Cu_2O that best reproduced empirical data, predicting a PBE+U/G_0W_0 gap (1.85 eV) with greater accuracy than LDA/G_0W_0 (1.34 eV [134]), although still slightly below experiment (2.17 eV [140]). Patrick and Giustino [150] applied the self-consistent method of Kioupakis et al. [36] to determine the $U-J$ value of anatase TiO_2, resulting in a $U-J$ of 7.5 eV that produced a PBE+U and PBE+U/G_0W_0 band gap of 3.27 eV. They applied the same $U-J$ to rutile TiO_2, which then also exhibited close agreement between the PBE+U and PBE+U/G_0W_0 gap. The PBE+U/G_0W_0 gaps are smaller than those predicted with DFT/G_0W_0 (rutile: 3.34, 3.59 eV; anatase: 3.56, 3.83 eV [135, 148]) and have worsened agreement with experiment for rutile, casting doubt on the fidelity of this approach for determining $U-J$. Jiang et al. [151] sampled a range of $U-J$ values for LDA+U/G_0W_0 with MnO, FeO, CoO, and NiO, showing that there was a strong dependence of the gap on $U-J$, likely due to the $U-J$–induced change in hybridization between O 2*p* and transition metal 3*d* orbitals. The band gaps reported in Table 3 for these four materials were calculated with $U-J$ obtained from constrained DFT-LDA, and agree well with experiment for CoO, but are underestimated for MnO and NiO. Nevertheless, the band gap predicted with LDA+U/G_0W_0 for NiO (3.75 eV) is a marked improvement over the LDA/G_0W_0 gap (1.0, 1.1 eV [120, 121]). The application of $U-J$ also causes the valence band in NiO to develop more O 2*p* character, in agreement with its description as a charge transfer insulator [122–129], due to the increased hybridization of the Ni 3*d* states with the O 2*p* states. The band gap prediction for MnO is improved with PBE+U/G_0W_0, with a $U-J$ of 3.54 derived from ab initio

Table 3 DFT+U eigenvalue gaps and DFT+U/G_0W_0 QP gaps for a number of transition and lanthanide metal oxides in comparison with experimental fundamental gaps. The exchange-correlation functional (LDA+U or PBE+U) is specified and the value used for $U-J$ is reported

	V_{xc}	$U-J$ (eV)	E_g(DFT+U) (eV)	E_g(DFT+U/G_0W_0) (eV)	E_g(Exp.) (eV)
TiO_2-rutile	PBE+U	7.5[a]	2.83[a]	2.85[a]	3.3 ± 0.5[b]
TiO_2-anatase	PBE+U	7.5[a]	3.27[a]	3.27[a]	3.4[c]
MnO	LDA+U	3.9[d]	1.54[d]	2.34[d]	3.9 ± 0.4[e]
MnO	PBE+U	3.54[f]	1.68[f]	3.07[f]	3.9 ± 0.4[e]
FeO	LDA+U	3.9[d], 3.7[g]	1.15[d], 1.6[g]	0.95[d], 1.6[g]	2.5[h]
Fe_2O_3	LDA+U	4.3[i]	1.9[i]	2.8[i]	2.6 ± 0.4[j]
Fe_2O_3	PBE+U	4.3[i]	2.2[i]	3.1[i]	2.6 ± 0.4[j]
CoO	LDA+U	4.2[d]	2.21[d]	2.47[d]	2.5 ± 0.3[k]
NiO	LDA+U	4.3[d]	2.90[d]	3.75[d]	4.3[l]
NiO	PBE+U	3.8[g]	–	3.60[g]	4.3[l]
Cu_2O	PBE+U	6.0[m]	0.74[m]	1.85[m]	2.17[n]
La_2O_3	LDA+U	5.4[o]	3.76[o]	4.95[o]	5.55[p], 5.34[q], 5.3[r]
Ce_2O_3	LDA+U	5.4[o]	2.24[o]	1.50[o]	2.4[p]
Pr_2O_3	LDA+U	5.4[o]	3.17[o]	2.86[o]	3.9[p], 3.5[q]
Nd_2O_3	LDA+U	5.4[o]	3.69[o]	4.50[o]	4.7[p], 4.8[q]
Pm_2O_3	LDA+U	5.4[o]	3.35[o]	5.25[o]	–
Sm_2O_3	LDA+U	5.4[o]	2.15[o]	4.38[o]	5.0[p]
Eu_2O_3	LDA+U	5.4[o]	1.28[o]	2.77[o]	4.4[p]
Gd_2O_3	LDA+U	5.4[o]	3.58[o]	4.89[o]	5.4[p]
Tb_2O_3	LDA+U	5.4[o]	3.34[o]	3.81[o]	3.8[p]
Dy_2O_3	LDA+U	5.4[o]	3.47[o]	4.41[o]	4.9[p]
Ho_2O_3	LDA+U	5.4[o]	3.05[o]	4.68[o]	5.3[p]
Er_2O_3	LDA+U	5.4[o]	2.69[o]	4.78[o]	5.3[p], 5.49[q]
Tm_2O_3	LDA+U	5.4[o]	1.73[o]	4.73[o]	5.4[p], 5.48[q]
Yb_2O_3	LDA+U	5.4[o]	1.25[o]	3.23[o]	4.9[p], 5.05[q]
Lu_2O_3	LDA+U	5.4[o]	3.18[o]	4.66[o]	5.5[p], 5.79[q], 4.89[s], 5.8[s]

[a] [150]; [b] [136]; [c] [137]*; [d] [151]; [e] [155]; [f] [152]; [g] [153]; [h] [156]; [i] [147]; [j] [149]; [k] [157]; [l] [139]; [m] [145]; [n] [140]*; [o] [154]; [p] [158]*; [q] [159]*; [r] [160]*; [s] [161]

UHF theory [152]. Similarly, using an ab initio $U-J$ somewhat improves the band gap predicted by LDA+U/G_0W_0 for FeO (0.95 eV from constrained DFT, 1.6 eV from ab initio DFT+U) [153]. Jiang et al. [154] also studied the dependence of G_0W_0 on $U-J$ for the lanthanide oxide series, where a relatively weak dependence on $U-J$ was observed within the range of meaningful values. They applied a constant value for $U-J$ of 5.4 eV to the entire lanthanide oxide series, chosen based on a physical estimate. The resulting LDA+U/G_0W_0 QP gaps reproduce some of the trends of the series, but many quantitative differences in the band gaps remain. Liao and Carter [147] used LDA+U/G_0W_0 and PBE+U/G_0W_0 to calculate the band gap in Fe_2O_3, and applied a $U-J$ of 4.3 eV derived from ab initio UHF theory [34, 35]. They found that LDA+U/G_0W_0 best reproduced the experimental

gap in comparison with all other implementations of GW, although PBE+U/G_0W_0 was relatively close in accuracy.

These results indicate that for many transition and lanthanide metal oxides, while DFT+U performs better that the standard DFT reference, the approximate treatment of exact exchange in DFT+U still does not adequately describe all electron–electron interactions. While the accuracy of DFT+U is somewhat influenced by the method used to derive $U-J$, in many materials these inadequacies persist at all meaningful $U-J$ values. The single G_0W_0 perturbation is ineffective in correcting the deficiencies of an inaccurate DFT+U reference. An improved reference wavefunction may be obtained from a DFT-based method with a less approximate incorporation of exact exchange.

3.2.3 Hybrid-DFT/G_0W_0

Hybrid functionals (such as PBE0, HSE, B3LYP, etc.) can also improve the description of electron–electron interaction by explicitly introducing a fraction of exact exchange. The nonlocal, screened exchange component of HSE functions similarly to the nonlocal and screened self-energy in the QP equation, so the use of HSE as a reference Hamiltonian can be viewed as a step toward self-consistency within the single perturbative approach. Consequently, HSE is the hybrid functional most widely used as the starting point for a single perturbative G_0W_0 approach.

The hybrid-DFT/G_0W_0 approach has been effective for most main group semiconductors and insulators, as the QP shifts in those cases are relatively small [162]. However, as apparent in the varying accuracy with transition metal oxides (Table 4), a consistent description of transition metal compounds is difficult within a hybrid-DFT/G_0W_0 approach. Cu_2O and MnO are the only materials studied where HSE/G_0W_0 accurately predicts the fundamental gap [145, 152] (note that the differences between the two results for the HSE and HSE/G_0W_0 gaps for MnO are likely due to these two studies using different implementations of the HSE functional, as the first study [163] employs the HSE03 functional, while the second study employs HSE06 [152]). For other materials (Fe_2O_3, CoO, and NiO [147, 162, 163]), the HSE/G_0W_0 QP gap is too large in comparison with experiment, and HSE/G_0W_0 often performs worse than DFT+U/G_0W_0. For FeO [163], the HSE/G_0W_0 gap is too low, although HSE/G_0W_0 is still a significant improvement over DFT+U/G_0W_0, as the greater component of exact exchange in HSE further increases the band gap. The HSE/G_0W_0 gap is also too low for ZnO [162], although it is an improvement over DFT/G_0W_0. The PBE0 reference typically increases the final G_0W_0 gap in comparison to an HSE reference due its larger contribution from HF exchange [145, 147], and generally worsens agreement with experiment (e.g., with Fe_2O_3 and Cu_2O).

Table 4 Hybrid-DFT eigenvalue gaps and hybrid-DFT/G_0W_0 QP gaps for a number of transition metal oxides in comparison with experimental fundamental gaps. The hybrid exchange-correlation functional is specified in the second column

	V_{xc}	E_g(hybrid-DFT) (eV)	E_g(hybrid-DFT/G_0W_0) (eV)	E_g(Exp.) (eV)
MnO	HSE	2.6[a], 3.07[b]	3.4[a], 3.82[b]	3.9 ± 0.4[c]
FeO	HSE	2.1[a]	2.2[a]	2.5[d]
Fe_2O_3	HSE	3.5[e]	4.0[e]	2.6 ± 0.4[f]
Fe_2O_3	PBE0	4.2[e]	4.5[e]	2.6 ± 0.4[f]
CoO	HSE	3.2[a]	3.4[a]	2.5 ± 0.3[g]
NiO	HSE	4.1[a]	4.7[a]	4.3[h]
Cu_2O	HSE	2.04[i]	2.17[i]	2.17[j]
Cu_2O	PBE0	2.84[i]	2.52[i]	2.17[j]
ZnO	HSE	2.11[k]	2.86[k]	3.37[l]

[a] [163]; [b] [152]; [c] [155]; [d] [156]; [e] [147]; [f] [149]; [g] [157]; [h] [139]; [i] [145]; [j] [140]*; [k] [162]; [l] [79]*

3.2.4 OEP-DFT/G_0W_0

An alternative to hybrid DFT is OEP with exact exchange (OEPx or OEPx(cLDA)), which approximates the non-local Fock operator via a local potential [37]. OEPx (cLDA)/G_0W_0 produced a band gap of 3.22 eV for wurtzite ZnO [164] in comparison to 3.37 eV from experiment [79], which is a marked improvement over the LDA/G_0W_0 (2.51 eV [121]) and PBE/G_0W_0 results (2.12 eV [146]).

3.3 *Self-Consistent* GW

The difficulty in obtaining a consistent description of transition metal oxides within a single G_0W_0 approach indicates that the effective application of G_0W_0 to these materials may require identification of a material-specific mean-field approach that best describes its properties. Alternatively, one may depart from the one-shot approach altogether, and strive to improve the *GW* prediction by introducing self-consistency when defining the self-energy and solving the QP equation. Self-consistency is extremely challenging to execute accurately. Fully self-consistent *GW* calculations on the homogeneous electron gas showed that self-consistency worsened agreement with experimental spectral properties [165]. This is because self-consistency introduces some higher order electron–electron interaction terms but lacks the higher order interaction terms included in the vertex function. Unless vertex corrections are included within fully self-consistent *GW*, non-self-consistent results are more accurate for most properties of the homogeneous electron gas. Fully self-consistent *GW* is also mathematically complex to execute, as the self-energy operator is non-local, non-Hermitian, and energy-dependent, and its resulting QP wavefunctions are non-orthonormal.

3.3.1 Self-Consistent Approximations for *GW*

To avoid the complexity of full self-consistency and its imbalanced treatment of higher order electron–electron interactions, a number of other strategies have been proposed that incorporate an approximation to the self-energy within a self-consistent scheme. Bruneval, Vast, and Reining [166] proposed a form which first applies the COHSEX approximation [117] to solve self-consistently for a static approximation to the self-energy, followed by a single perturbative G_0W_0 step. The self-energy can be divided into two parts: a dynamically screened exchange operator (SEX) and a Coulomb hole (COH) term. SEX is similar to the Fock operator in HF theory, but the bare Coulomb potential v has been replaced by the screened Coulomb potential W. COH represents the induced response of the electrons of the system to an added or removed point charge. COHSEX employs a static approximation for SEX, where screening is assumed to be instantaneous, such that only occupied states contribute to the term. Additionally, the COH term is reduced to a local screening potential. The self-energy contributions from these terms are both Hermitian and energy-independent, and therefore result in orthogonal QP wavefunctions. Self-consistency within COHSEX is an approximation to self-consistent *GW*, but because it completely neglects dynamical screening, dynamical effects are introduced afterward via the single G_0W_0 perturbation.

The self-consistent COHSEX method with a single perturbative G_0W_0 has been used in calculating the spectral properties of VO_2 [119]. VO_2 has a band gap of 0.2–0.7 eV from experiment [138], but LDA/G_0W_0 fails to open up any gap. However, self-consistent COHSEX on its own opens up a gap of 0.78 eV, and the final G_0W_0 perturbation results in a gap of 0.65 eV. In this case, the change in the wavefunctions from the LDA wavefunctions was essential to open up the gap.

Another approximation to the self-energy within self-consistent *GW* is the model *GW* (m*GW*) approach proposed by Gygi and Baldereschi [167]. Here, the self-energy is split into a short range part that is approximated by the LDA, and a long range correction that is approximated by a model dielectric function. This approach is not completely free from empiricism, as the approximate model dielectric function requires an input value for the dielectric constant, which is frequently taken from experiment.

Table 5 shows the band gaps of selected transition metal oxides as calculated with m*GW*. m*GW* for NiO [168, 169] is a definite improvement over LDA/G_0W_0 (1.0, 1.1 eV [120, 121]), although it predicts a gap like DFT+U/G_0W_0 (3.75, 3.60 eV [151, 153]) and is still below experiment. It also describes the character of the top of the valence band correctly, showing significant contributions from O 2*p* states [169], similar to the band character predicted in LDA+U/G_0W_0 [151]. m*GW* succeeds in opening up a gap in VO_2 [170], with accuracy nearly equivalent to COHSEX/G_0W_0 (0.65 eV [119]). For MnO, FeO, and $CaCuO_2$ [168, 169], m*GW* predicts fundamental gaps very close to experiment, exhibiting significant improvements from previous DFT+U/G_0W_0 calculations for MnO (2.34, 3.07 eV [151, 152]) and FeO (0.95, 1.6 eV [151, 153]). However, the band gaps from m*GW* are overestimated for CoO and ZnO [168, 171], indicating that while its approximations are successful for many materials, it is still not a universally accurate method.

Table 5 QP gaps calculated with model *GW* (m*GW*) [167] for a number of transition metal oxides in comparison with experimental fundamental gaps

	E_g(m*GW*)	E_g(Exp.)
VO_2	0.6[a]	0.2–0.7[b]
MnO	4.2[c], 4.03[d]	3.9 ± 0.4[e]
FeO	2.32[d]	2.5[f]
CoO	3.02[d]	2.5 ± 0.3[g]
NiO	3.7[h], 3.60[d]	4.3[i]
$CaCuO_2$	1.4[h]	1.5[j]
ZnO	4.23[k]	3.37[l]

[a] [170]; [b] [138]; [c] [172]; [d] [168]; [e] [170]; [f] [156]; [g] [156]; [h] [169]; [i] [139]; [j] [173]*; [k] [171]; [l] [79]*

3.3.2 Self-Consistent Diagonal GW_0 and GW

Another approach to self-consistency uses the standard *GW* formalism for calculating the self-energy but considers only its diagonal elements, thereby employing an energy-only self-consistent approach where only the eigenvalues are updated in successive iterations of a G_0W_0-like perturbation. The updated eigenvalues can be used to recalculate both G and W at every iteration (denoted GW) or only to update G, keeping W fixed as W_0 (denoted GW_0). This procedure avoids the problems with non-Hermiticity of the self-energy and the ensuing non-orthonormal wavefunctions by fixing the wavefunctions to the initial KS-DFT input. Because the wavefunctions are kept fixed, this method is not completely independent of the starting guess, and a range of mean-field theories have been used to generate reference wavefunctions.

Table 6 shows the band gaps of selected transition metal oxides as calculated with self-consistent GW_0 and/or GW, using wavefunctions generated with a number of exchange-correlation functionals. Typically, introducing self-consistency with GW_0 or GW results in larger gaps than with a single G_0W_0 perturbation. This trend occurs in HSE/GW and PBE/GW with ZnO [146, 162], LDA+U/GW_0 with MnO, CoO, and NiO [151], LDA/GW with Cu_2O [134], and LDA+U/GW_0 with many of the lanthanide oxide series [154]. In these studies, the increase in QP gaps also often improves agreement with experimental band structures and fundamental gaps. However, while there is some improvement in accuracy, in many cases there are still significant quantitative differences, likely due to the enduring influence of an inaccurate reference Hamiltonian. In Fe_2O_3 [147] the increasing levels of self-consistency further opened up the gap, but led to worsened agreement with experiment for reference Hamiltonians with larger initial eigenvalue gaps. And in other cases, increasing levels of self-consistency resulted in decreased band gaps, such as in LDA/GW_0 with FeO [151] and Ce_2O_3, Pr_2O_3, Tb_2O_3, and Dy_2O_3 of the lanthanide oxides [154]. Overall, these results show that introducing self-consistency in this manner is not a panacea to the problems in the G_0W_0 approach, as the success of the self-consistent GW_0 and GW methods is still dependent on both the material and the reference Hamiltonian.

Table 6 QP gaps calculated with self-consistent GW_0 and/or GW for a number of transition and lanthanide metal oxides in comparison with experimental fundamental gaps. The exchange-correlation functional used in the reference Hamiltonian, H_0, is specified in the second column. The eigenvalue gaps of the reference Hamiltonian, $E_g(H_0)$, are reported when available and the values of $U-J$ are reported where appropriate

	V_{xc}	$U-J$ (eV)	$E_g(H_0)$ (eV)	$E_g(H_0/GW_0)$ (eV)	$E_g(H_0/GW)$ (eV)	E_g(Exp.) (eV)
TiO_2-rutile	PBE+U	3.0[a]	–	–	4.48[a]	3.3 ± 0.5[b]
V_2O_3	PBE+U	3.0[a]	–	–	1.70[a]	0.2[c]
VO_2	PBE+U	3.0[a]	–	–	1.12[a]	0.2–0.7[d]
V_2O_5	PBE+U	3.0[a]	–	–	4.69[a]	2.15[e]
Cr_2O_3	PBE+U	3.0[a]	–	–	4.75[a]	4.7–5.0[f]
MnO	LDA+U	3.9[g]	1.54[g]	2.57[g]	–	3.9 ± 0.4[h]
MnO	PBE+U	3.0[a]	–	–	3.81[a]	3.9 ± 0.4[h]
Mn_3O_4	PBE+U	3.0[a]	–	–	2.89[a]	2.5[i]
FeO	LDA+U	3.9[g]	1.15[g]	0.86[g]	–	2.5[j]
FeO	PBE+U	3.0[a]	–	–	1.65[a]	2.5[j]
Fe_2O_3	PBE	–	0.6[k]	1.7[k]	1.8[k]	2.6 ± 0.4[l]
Fe_2O_3	LDA+U	4.3[k]	1.9[k]	3.3[k]	4.0[k]	2.6 ± 0.4[l]
Fe_2O_3	PBE+U	4.3[k]	2.2[k]	3.6[k]	4.3[k], 3.57[a]	2.6 ± 0.4[l]
Fe_2O_3	HSE	–	3.5[k]	4.4[k]	4.7[k]	2.6 ± 0.4[l]
Fe_2O_3	PBE0	–	4.2[k]	4.7[k]	4.8[k]	2.6 ± 0.4[l]
CoO	LDA+U	4.2[g]	2.21[g]	2.54[g]	–	2.5 ± 0.3[m]
CoO	PBE+U	3.0[a]	–	–	3.23[a]	2.5 ± 0.3[m]
Co_3O_4	PBE+U	3.0[a]	–	–	2.42[a]	1.6[n]
NiO	LDA+U	4.3[g]	2.90[g]	3.76[g]	–	4.3[o]
NiO	PBE+U	3.0[a]	–	–	4.28[a]	4.3[o]
Cu_2O	LDA	–	0.54[p]	–	1.80[p]	2.17[q]
Cu_2O	PBE+U	5.0[a]	–	–	1.59[a]	2.17[q]
CuO	PBE+U	3.0[a]	–	–	2.49[a]	1.4[r]
ZnO	PBE	–	0.67[s]	2.54[s]	3.20[s]	3.37[t]
ZnO	HSE	–	2.11[u]	3.02[u]	3.33[u]	3.37[t]
La_2O_3	LDA+U	5.4[v]	3.76[v]	5.24[v]	–	5.55[w], 5.34[x], 5.3[y]
Ce_2O_3	LDA+U	5.4[v]	2.24[v]	1.29[v]	–	2.4[w]
Pr_2O_3	LDA+U	5.4[v]	3.17[v]	2.82[v]	–	3.9[w], 3.5[x]
Nd_2O_3	LDA+U	5.4[v]	3.69[v]	4.70[v]	–	4.7[w], 4.8[x]
Pm_2O_3	LDA+U	5.4[v]	3.35[v]	5.41[v]	–	–
Sm_2O_3	LDA+U	5.4[v]	2.15[v]	5.22[v]	–	5.0[w]
Eu_2O_3	LDA+U	5.4[v]	1.28[v]	3.48[v]	–	4.4[w]
Gd_2O_3	LDA+U	5.4[v]	3.58[v]	5.30[v]	–	5.4[w]
Tb_2O_3	LDA+U	5.4[v]	3.34[v]	3.74[v]	–	3.8[w]
Dy_2O_3	LDA+U	5.4[v]	3.47[v]	4.24[v]	–	4.9[w]
Ho_2O_3	LDA+U	5.4[v]	3.05[v]	5.12[v]	–	5.3[w]
Er_2O_3	LDA+U	5.4[v]	2.69[v]	5.22[v]	–	5.3[w], 5.49[x]
Tm_2O_3	LDA+U	5.4[v]	1.73[v]	5.15[v]	–	5.4[w], 5.48[x]
Yb_2O_3	LDA+U	5.4[v]	1.25[v]	4.70[v]	–	4.9[w], 5.05[x]
Lu_2O_3	LDA+U	5.4[v]	3.18[v]	4.99[v]	–	5.5[w], 5.79[x], 4.89[z], 5.8[z]

[a] [174]; [b] [136]; [c] [175]; [d] [138]; [e] [176]*; [f] [177]*; [g] [151]; [h] [155]; [i] [178]*; [j] [156]; [k] [147]; [l] [149]; [m] [157]; [n] [179]; [o] [139]; [p] [134]; [q] [140]*; [r] [180]*; [s] [146]; [t] [79]*; [u] [162]; [v] [154]; [w] [158]*; [x] [159]*; [y] [160]*; [z] [161]

Table 7 QP gaps calculated with the QPscGW method [181] for several transition metal oxides in comparison with experimental fundamental gaps

	E_g(QPscGW) (eV)	E_g(Exp.) (eV)
MnO	3.5[a]	3.9 ± 0.4[b]
Fe_2O_3	2.9, 3.5, 4.2, 4.3[c]	2.6 ± 0.4[d]
NiO	4.8[a]	4.3[e]
Cu_2O	1.97[f]	2.17[g]

[a] [181]; [b] [155]; [c] [147], where the four values result from reference Hamiltonians of PBE, LDA+*U*/PBE+*U*, HSE, and PBE0, in that order; [d] [149]; [e] [139]; [f] [134]; [g] [140]*

3.3.3 Self-Consistent Hermitized *GW*

Truly self-consistent methods should not be influenced by the choice of reference Hamiltonian. However, the challenge of such self-consistent methods that update both the eigenvalues and wavefunctions is to resolve somehow the non-Hermiticity of the self-energy. The QP self-consistent *GW* (QPscGW) method of Faleev, van Schilfgaarde, and Kotani [181] constrains the dynamical self-energy so that it becomes static and Hermitian by symmetrizing the off-diagonal elements to regularize the self-energy. This constrains the resulting Hamiltonian to be Hermitian while the self-energy remains as close as possible to the original self-energy.

The QPscGW method should be free from any dependence on the input wavefunction; however, its application (Table 7) to Fe_2O_3 showed significant differences in the band gap with varying initial DFT references, indicating that the choice of input wavefunction can lead to a solution that is a local minimum [147]. Overall, QPscGW showed worsened agreement with experiment for the band gap of Fe_2O_3, and the recommended method was DFT+U/G_0W_0. For NiO, the band gap is more significantly overestimated with QPscGW than with any of the previous *GW* methods, and there are some discrepancies between PE experiments and the QP spectrum [181]. QPscGW on MnO [181] provides a value at the lower bound of the experimental gap (3.5 eV), which is an improvement over the DFT+U/G_0W_0 calculations (2.34, 3.07 eV [151, 152]), although one HSE/G_0W_0 calculation (3.82 eV [152]), model *GW* (4.2, 4.03 eV [168, 172]), and PBE+U/*GW* (3.81 eV [174]) performed better. Similarly, the QPscGW gap for Cu_2O [134] is more accurate than the gaps calculated with most other *GW* methods (1.34, 1.39, 1.85, 2.52 eV [134, 145]), excluding HSE/G_0W_0 (2.17 eV [145]). Consequently, self-consistency with QPscGW is also not a universally reliable method, as its accuracy is material-specific and still appears to depend on the input wavefunction.

Sakuma, Miyake, and Aryasetiawan [182] proposed another form of self-consistent *GW* to update both the eigenvalues and wavefunctions, called the QPM approximation. Their self-consistent procedure begins with a *GW* calculation built on LDA input, and the resulting QP wavefunctions are then orthogonalized by diagonalizing a Hermitian QP Hamiltonian constructed from the QP eigenvalues and corresponding QP wavefunction projectors. This can be run self-consistently, but, due to the expense, they approximated self-consistency by introducing a shift to the conduction band QP energies, chosen such that the input and output band gaps

are equivalent. They applied this approach to VO_2 and found a gap of 0.6 eV in comparison to 0.2–0.7 eV from experiment [138]. The QPM approximation was a precursor to their later scheme for self-consistent *GW*, which constructs a Hermitian Hamiltonian using Lowdin's method of symmetric orthogonalization, thus ensuring the orthonormality of the orbitals [183]. This form of self-consistent *GW* was applied to NiO, which yielded a band gap of ~5 eV, which is greater than the experimental gap of 4.2 eV. The predicted band structure matches the QPscGW band structure nearly exactly, indicating the similarity between these two methods. The overestimation of the band gap within many self-consistent forms of *GW* has been attributed to the lack of higher-order many-body correlation effects when applying self-consistency [184], underscreening by the RPA [185], or the neglect of the contribution of lattice polarization to the screening of the electron–electron interaction [186, 187]. However, these self-consistent schemes may be viewed as a good mean field starting point for those higher-order calculations.

3.4 GW *Outlook*

An overview of the performance of all *GW* methods is shown in Fig. 3. This review of the many implementations of *GW* shows that there is no universal *GW* method appropriate for all transition metal oxides. *GW* is also hindered by its computational expense, largely due to the nonlocality and frequency dependence of the self-energy operator and its slow convergence with respect to k-point sampling and the number of empty bands. It has been shown that the band gap may not completely converge, even with hundreds of empty bands [188]. *GW* also scales as $O(N^4)$. Technical improvements to the execution of *GW* and more formal theoretical improvements such as vertex corrections or models that account for lattice polarization may increase progress towards an efficient and accurate universal approach, thus improving the description of transition metal oxides.

3.5 Bethe–Salpeter Equation

To describe the neutral excitations that occur in absorption spectroscopy and to derive the optical gap, a theory needs to account for the screened electron–hole interaction involved in the formation of excitons. This interaction is described in the Bethe–Salpeter equation (BSE) [98, 189, 190], which solves for the neutral excitation energies as the poles of the two-particle Green's function. The solution of the BSE typically begins with a *GW* calculation to solve for the quasielectron and quasihole. BSE theory then subsequently introduces an interaction term that mixes the two types of charged transitions. The BSE can be extremely computationally demanding, as it requires an even larger number than *GW* of empty bands and k-points to obtain converged results. BSE also scales as $O(N^5)$, which presents a computational

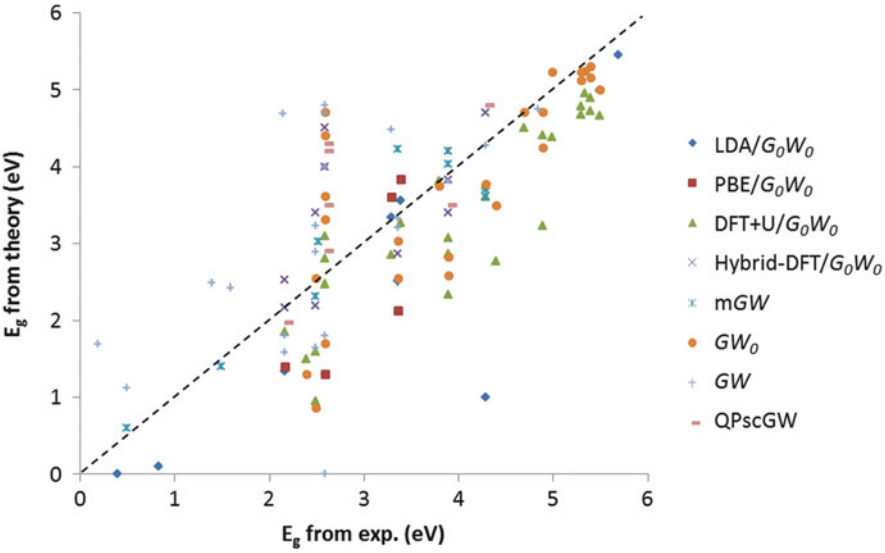

Fig. 3 A graphical representation of the data presented in Tables 1, 2, 3, 4, 5, 6, and 7, showing the collected computed vs experimental band gaps for all materials and methods considered

challenge for systems larger than 100 atoms, even when massively parallelized. One approach decreases the computational expense by generating the necessary electronic states with an approximation to *GW* in which a GGA+*U* calculation with a scissor shift operator (GGA+*U*+*Δ*) is used to reproduce a less refined approximation of the *GW* band structure [191, 192]. Another approximation to BSE was developed by Reining and coworkers [99, 193–195], who derived an effective nonlocal exchange-correlation kernel from the BSE to reproduce excitonic effects (first applied within a TD-DFT context and then subsequently extended to *GW/BSE*), which accounts for both self-energy corrections as well as the screened electron–hole interaction.

The GGA+*U*+*Δ* approximation was used to generate input for BSE calculations on ZnO, CdO, MnO, FeO, CoO, and NiO [191, 192]. For these materials, the inclusion of excitonic effects was shown to be necessary to obtain agreement with experimental absorption peak positions. BSE calculations enabled relevant peaks in the optical spectrum to be characterized as specific optical interband transitions. The approximation to the BSE using the kernel developed by Reining et al. was applied to a number of materials [196], and an optical gap of 3.2 eV was predicted for ZnO in comparison to 3.3 eV from experiment [197]. Here, the vertex corrections were only used in the construction of *W*, but were neglected in the construction of Σ due to numerical instabilities. The BSE without any approximations was used in calculations of Cu_2O [134], which appropriately described the strong excitonic effects of the material. BSE produces a detailed absorption spectrum (Fig. 4) that is useful in analyzing the experimental spectrum. BSE was also used to model rutile and anatase TiO_2 [135, 148]. The optical gap for rutile

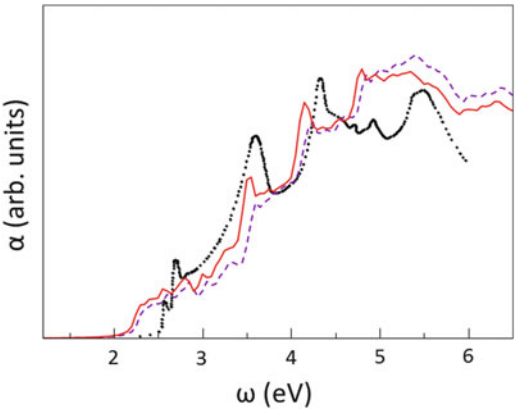

Fig. 4 Optical absorption spectrum of Cu_2O from experiment (*black dotted line*), from BSE with QPscGW input and an LDA dielectric function (*purple dashed line*), and from BSE with QPscGW input and a QPscGW dielectric function (*red solid line*). Reprinted with permission from Bruneval F, Vast N, Reining L, Izquierdo M, Sirotti F, Barrett N, Phys Rev Lett, 97, 267601, 2006. Copyright (2006) by the American Physical Society

TiO_2 was predicted to be 3.25 eV, which is only 0.22 eV above experiment, and the overall optical spectrum for rutile TiO_2 was shifted by only 0.1–0.2 eV with respect to experiment.

Overall, the BSE has been shown to be a powerful tool in analyzing optical absorption spectra, but its greatest challenge is its computational expense. While the various approximations to BSE help reduce this burden, other theoretical approaches may be helpful in studying neutral excitations with less of a computational load.

4 Embedded Correlated Wavefunction Methods

GW and BSE theories are typically applied to bulk crystalline materials, and the resulting spectra are therefore interpreted according to band theory. While this approach describes delocalized excitations in the continuum very well, it is also important to characterize localized excitations that involve only selected atoms and orbitals, especially in materials where optical excitations of multiple characters may occur. The localized neutral excitations that may occur in optical spectroscopy can be better described by theories designed to model neutral excited states in more localized models. To this end, we turn to correlated wavefunction methods, which can easily characterize ground and excited states in clusters. The optical gap can be obtained as the difference between the lowest excited state energy and the ground state energy, and similarly, the entire optical absorption spectrum can be derived from a series of excited state energies and oscillator strengths. The character of the localized excitations can be probed through explicit models of their electronic structure.

4.1 Correlated Wavefunction Theory

Many-electron wavefunction methods solve for the electronic structure of a system using an ansatz of a wavefunction that is variationally optimized to solve the Schrödinger equation. Within the Born–Oppenheimer approximation, the electronic wavefunction is solved for in the field of fixed nuclei, where the electronic Hamiltonian of the time-independent Schrödinger equation consists of the kinetic energy operator, an electron-nuclear attraction operator, and the electron–electron repulsion operator:

$$\begin{aligned}\hat{H}\,\Psi(\mathbf{r}_1 \ldots \mathbf{r}_N) &= \sum_{i=1}^{N}\left(-\frac{1}{2}\nabla^2\Psi - \sum_A Z_A \frac{1}{|\mathbf{r}_i - \mathbf{R}_A|}\Psi\right) + \frac{1}{2}\sum_{i\neq j}\frac{1}{|\mathbf{r}_i - \mathbf{r}_j|}\Psi \\ &= E\Psi \end{aligned} \tag{16}$$

HF theory [198, 199], essentially variational molecular orbital theory, is the starting point for most quantum chemistry methods. HF theory approximates the many-electron wavefunction as a single Slater determinant of one-electron spin-orbitals, which fulfills the requirement of wavefunction antisymmetry with respect to permutation of electrons (i.e., the Pauli Exclusion Principle):

$$\Psi(\mathbf{r}_1 \ldots \mathbf{r}_\mathbf{N}) = \begin{vmatrix} \phi_1(\mathbf{r}_1) & \phi_2(\mathbf{r}_1) & \ldots & \phi_N(\mathbf{r}_1) \\ \phi_1(\mathbf{r}_2) & \phi_2(\mathbf{r}_2) & \ldots & \vdots \\ \vdots & \vdots & \vdots & \vdots \\ \phi_1(\mathbf{r}_N) & \ldots & \ldots & \phi_N(\mathbf{r}_N) \end{vmatrix} \tag{17}$$

The many-body wavefunction is solved for by applying a self-consistent mean-field approximation, where each electron is subjected to an averaged Coulomb potential and an exchange operator due to all other electrons. The exchange interactions arise from the required permutational antisymmetry of the many-electron wavefunction, and their explicit form is dictated by the Slater determinant wavefunction. HF theory scales as $O(N^4)$, although the scaling for the overall calculation can be lowered by using a screening method for the two-electron integrals [200–206]. The scaling for the calculation of the Fock matrix can also be reduced to linear using hierarchical multipole expansions [207–210]. HF can be applied to systems with several hundred atoms.

While Coulomb and exchange interactions are accounted for exactly within HF theory, because of the constraint of a single-determinant solution, the HF solution does not account for any electron correlation. A single electron configuration (a single determinant) wavefunction is insufficient for describing situations where so-called static electron correlation is important, such as when the ground state is best described with more than one (nearly) energy degenerate determinant. Moreover, correlating electron motion lowers electron–electron repulsion, which leads to a lower total energy that will be closer to the exact solution.

Møller–Plesset perturbation (MPn) theory [211] is the simplest method of introducing electronic correlation. MPn theory treats the full Hamiltonian as a perturbed independent electron Hamiltonian, using the ground state HF wavefunction and Fock operator as the starting point. MPn theory builds in so-called dynamic correlation, in which correlated motion of the electrons is accounted for via electronic excitations from the ground state wavefunction. One of the most commonly used forms is MP2, where the energy is expanded to a second order perturbation. The MP2 second order energy is expressed using the HF orbitals and eigenvalues as

$$E_{\mathrm{MP2}} = \frac{1}{4}\sum_{ij}^{\mathrm{occ}}\sum_{ab}^{\mathrm{virt}} \frac{\left|\langle \phi_i \phi_j | r_{12}^{-1} | \phi_a \phi_b \rangle\right|^2}{\varepsilon_i + \varepsilon_j - \varepsilon_a - \varepsilon_b}. \tag{18}$$

MP2 formally scales as O(N^5), although linear-scaling methods have been designed [212–216], so that MP2 is not a significant increase from the computational expense of HF. MP2 is also size-consistent. Unfortunately, MP2 is not variational, so the calculated correlation energy may be too large.

Static correlation is treated explicitly with a self-consistently optimized multi-configurational wavefunction that includes all significant, nearly-degenerate determinants in the wavefunction. An example of a multi-configurational approach is the Complete Active Space Self-Consistent Field (CASSCF) method [217]. The CASSCF wavefunction is a linear combination of configuration state functions (CSFs; spin and spatial symmetry-adapted linear combinations of Slater determinants) generated by distributing a subset of electrons in all possible ways within an active subset of the orbital space:

$$\Phi = \sum_K A_K \Psi_K \tag{19}$$

The total energy is minimized with respect to both the molecular orbital coefficients and the expansion coefficients A_K. One of the greatest challenges of the CASSCF method is choosing the active space of electrons and orbitals. Ideally, one would like to include the full valence space; however, CASSCF scales factorially with respect to the number of active orbitals and electrons. Including the full valence space is therefore not feasible in larger systems, as the practical upper limit to the active space is typically 16 electrons in 16 orbitals. Instead, the active space can be selected according to a set of guiding criteria [218]. The most important orbitals to include in the active space are those that would be likely to have fractional occupations on average. Additionally, when modeling systems containing transition metals, all orbitals of *d*-character should typically be included. Unfortunately, even following these basic guidelines for selecting the prime candidates for the active space frequently results in an active space size that is computationally impractical and must be further truncated. The success of CASSCF largely depends on the choice of the active space. While CASSCF is effective for treating static correlation,

it does not account for dynamic correlation. However, the CASSCF wavefunction is often used as a very good starting point for other levels of theory that introduce dynamic correlation. For instance, CASPT2 [219] is a second order perturbation theory approach to dynamic correlation based on a CASSCF reference state.

Configuration interaction (CI) [220] is frequently used for the explicit introduction of dynamic correlation. The CI wavefunction is a linear combination of CSFs whose determinants are defined by excitations from one (or more) reference determinants, typically the HF determinant. Full CI includes all possible determinants formed by exciting any number of electrons from the occupied to unoccupied states in the reference determinant Ψ_0 within the set of spin orbitals:

$$|\Phi_0\rangle = c_0|\Psi_0\rangle + \sum_{ar} c_a^r \left|\Psi_a^r\right\rangle + \sum_{a<b,r<s} c_{ab}^{rs} \left|\Psi_{ab}^{rs}\right\rangle + \sum_{a<b<c,r<s<t} c_{abc}^{rst} \left|\Psi_{abc}^{rst}\right\rangle + \sum_{a<b<c<d,r<s<t<u} c_{abcd}^{rstu} \left|\Psi_{abcd}^{rstu}\right\rangle + \ldots \tag{20}$$

A variationally optimized full CI expansion that uses a complete set of spin orbitals would produce the exact nonrelativistic ground state energy. Because an infinite basis set cannot be handled, a finite set of spin orbitals must be used. Full CI within this subspace is still intractable (scaling factorially), so CI approaches instead typically use a small fraction of all possible determinants by truncating the expansion of (20). The first order truncation includes single excitations only, which is not helpful in improving the description of the ground state wavefunction, but can be used to describe excited states in the so-called CI Singles (CIS) approach [221]. A popular truncation is at second order to include single and double excitations (SDCI), as excitations greater than those do not couple directly to the reference determinant. A single reference determinant is insufficient in cases where static correlation is significant, and in those instances the CI wavefunction can be constructed via excitations from more than one reference wavefunction. CI with single and double excitations from more than one reference is called multi-reference SDCI or MRSDCI, where the reference determinants are typically chosen by identifying the dominant references in a prior CASSCF calculation. MRSDCI typically scales as $O(N^6)$, limiting these calculations to relatively small systems, though again reduced scaling algorithms exist that allow larger numbers (though not hundreds) of atoms to be treated [222–224]. Truncated CI energies are upper bounds to the energies of a system, as CI theory is variational. Excited states within CI correspond to higher order eigenvalue and eigenfunction solutions of the (typically) nonrelativistic Hamiltonian eigenvalue problem. A major drawback of CI theory is that, while full CI is theoretically size extensive, truncated CI expansions are not size extensive, and therefore accuracy will decrease with increasing system size.

An alternative to CI is coupled cluster (CC) theory [225], which constructs a multi-determinant wavefunction consisting of a linear combination of excited Slater determinants using an exponential excitation operator that acts on the HF reference:

$$|\Phi_0\rangle = e^{\hat{T}}|\Psi_0\rangle \tag{21}$$

where $\hat{T}$ is the excitation operator

$$\hat{T} = \hat{T}_1 + \hat{T}_2 + \hat{T}_3 \ldots \tag{22}$$

and $\hat{T}_1$ is the operator for all single excitations, $\hat{T}_2$ is the operator of all double excitations, etc. Typically, the cluster operator is truncated at or before the triple excitation operator. However, if the CC expansion is truncated, CC theory is no longer variational and the computed energy will not be an upper bound to the true energy of the system. A variant of CC theory called equation-of-motion CC (EOM-CC) [226] is used to calculate excited states, where the excited state wavefunction is generated from a reference state by the action of an excitation operator. EOM-CC including single and double excitations scales as $O(N^6)$, generally limiting these methods to fairly small, gas phase systems (molecules).

These correlated wavefunction methods are very powerful for calculating ground and excited state properties. However, their high level of accuracy is compromised by their high computational cost, and it is not yet possible to use these methods routinely to treat condensed matter due to their prohibitive expense, though periodic MP2 [227–234] and coupled cluster theories [235, 236] have been developed. A crude approximation to model an extended system, such as a bulk crystal or surface, is as an isolated cluster. This method removes the impact of the environment on the cluster, whose influence may be non-negligible. A more accurate approach is to partition the system into a region of interest, which is treated with the higher level correlated wavefunction method, and its environment, which is treated with some lower level method (Fig. 5). This partitioning assumes that the impact of the environment is non-negligible but slightly less important, justifying its treatment with a lower level of theory. The influence of the environment on the region of interest is incorporated in the correlated wavefunction method as an embedding potential.

4.2 Electrostatic Embedding

The simplest embedding model represents the background as a point charge array. This representation is only appropriate for ionic systems, where the electron density is relatively localized and the long-range interactions between the cluster and environment can be approximated as purely electrostatic. Therefore this approach is not well suited for some transition metal oxides containing more covalent character. Correlated wavefunction theory must operate in finite real-space, so the point charge array is often constructed as a finite array. However, the Madelung potential of a finite array converges slowly in real space with respect to array size, which may lead to significant deviations from the exact Ewald potential of the

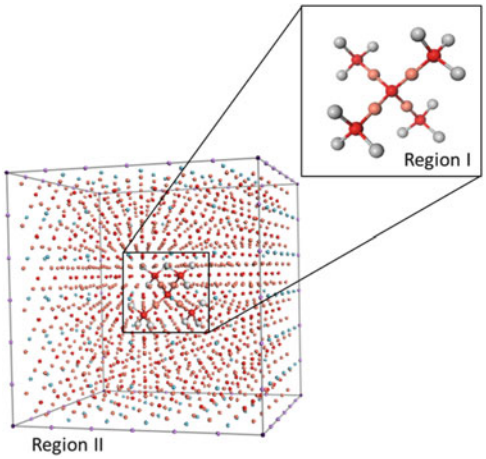

Fig. 5 Schematic of the embedding approach to modeling extended materials, illustrated here with Cu_2O. *Region I* is the embedded cluster, treated with the higher-level correlated wavefunction theory, while *Region II* is the environment, treated with a lower level of theory. The effect of Region II on Region I is incorporated into the correlated wavefunction theory calculation as an embedding potential that is an additional one-electron operator in the Hamiltonian

periodically infinite crystal. Therefore, the appropriate size and shape of the point charge array must be chosen to properly converge the Madelung potential. The standard approach is Evjen's method [237], which defines fractional charges for point charges in the terminal positions of an array with the same symmetry as the bulk unit cell. In a cuboid array, for example, Evjen's method assigns one eighth of the bulk charge on point charges at the vertices, one quarter of the bulk charge on point charges at edges, and one half of the bulk charge on point charges on faces. There are alternate procedures to construct the background potential, such as the periodic electrostatic embedded cluster method, which uses the periodic fast multipole method to provide the correct Madelung potential due to a periodic array of point charges [238]. Still other approaches define auxiliary charges to represent the Madelung potential [239, 240].

When defining the point charge array according to Evjen's method, the point charge values are typically derived from the formal oxidation numbers of the ionic compound. However, the formal charges may not accurately reflect the physical ionicity of the compound, which can demonstrate partial ionicity. The use of overly high charges in the background array is therefore an unphysical representation that may lead to excessive polarization of the electron density in the quantum mechanical (QM) cluster. A better approach may be to use a more physical value that more accurately represents the material's ionicity, where point charges values can be obtained via a prior charge partitioning scheme such as Mulliken charges [241], Löwdin charges [242], Hirshfeld [243] charges, or Bader charges [244–247] from periodic DFT or HF calculations. A number of calculations suggest that using the more physical fractional values in the point charge arrays is more appropriate [248–250].

When the QM cluster is immediately surrounded by a point array, the boundary atoms of the cluster that neighbor positive point charges of the environment experience a strong artificial distortion of their electron density [251]. To prevent this artificial drift of the electron density, the positive point charges adjacent to the cluster are typically replaced by effective core potentials (ECPs), which restore the missing short range Pauli repulsion between the cluster and its immediate environment [251–253].

A more extensive representation of the background array is to use ab initio model potentials (AIMPs) instead of point charges [254, 255]. AIMPs have an advantage over ECPs in that they can be used to represent anions in addition to cations. AIMPs can be used to represent the complete background array, or can be used to replace point charges only in the region immediately surrounding the cluster as a means of preventing the artificial drift of the electron density.

A fixed point charge array may be inappropriate in cases where polarization of the environment is important. Environmental polarization can be introduced by partitioning the background into two regions, where the region immediately surrounding the cluster is treated with the polarizable shell model [256, 257]. In this region, polarizability is introduced by representing the anions as a positive point charge to which a negatively-charged shell is connected via a harmonic potential. The polarizable environment is allowed to respond to electronic distortions (e.g., excitations) within the QM cluster, while the rest of the non-polarizable point charge array is held fixed. A similar approach is the elastic polarizable environment model [258], where the environment is partitioned into three regions: a shell model region, a point charge region, and a dielectric continuum. These methods that incorporate a polarizable region may also include ECPs at the cluster boundary to prevent spurious charge drift.

Point charge and AIMP embedding are the most widely used approaches in embedded cluster methods applied to transition metal oxides. Thus far, all applications of point charge embedding for transition metal oxides obtained point charge values from formal oxidation numbers as opposed to fractional ionicities. One use of these embedded correlated wavefunction methods has been to characterize absorption spectra and evaluate its contributing *d*–*d* transitions. De Graaf et al. [259] modeled the neutral *d*–*d* excitations in NiO using CASSCF/CASPT2 and point charge embedding, producing excitation energies that compare well to experiment. Another study of the NiO absorption spectrum, performed by Domingo et al. [260], used CASSCF/CASPT2 with a direct reaction field [261] to allow for polarization of the environment. In this model, AIMPs and point charges are used with added induced electric dipoles, where the polarizabilities of the atoms are assigned based on empirical values. Here, the theoretical spectrum reproduced the experimental spectrum, helping to pinpoint some of the origins of its features. For instance, the origin of the optical gap at 4.1 eV was identified as being due to a ligand-to-metal charge transfer, confirming the charge transfer nature of NiO. The polarized environment helped to explain the source of broadening and relaxation of charge transfer states. Liao and Carter [262] studied the lowest optical excitations in Fe_2O_3 using CASSCF/CASPT2 with the cluster embedded in a point charge array.

They characterized the lowest excitations as *d–d* transitions that start at ~2.5 eV, while ligand to metal charge transfer excitations occur at higher energies starting at ~6 eV. The optical band gap of Fe_2O_3 is 2.0–2.2 eV [263], and so the embedded cluster model slightly overestimates the optical gap. De Graaf and Broer [264] studied the *d–d* transitions in a series of cuprates with embedded CASSCF/CASPT2, to analyze the effect of copper coordination on *d–d* transition energies. Their embedding model used a point charge array, where the point charges at the cluster boundary were replaced with AIMPs. They found the lowest *d–d* transition to be 1 eV or higher in all cuprates, where the only transition that changed throughout the series is $3d_{x^2-y^2} \rightarrow 3d_{z^2}$ transition, due to changes in coordination along the *z*-axis. Kanan and Carter [265] examined *d–d* and charge-transfer excitations to explain the optical absorption spectrum of pure MnO and a MnO:ZnO alloy. Their study used electrostatically embedded cluster models and CASSCF/CASPT2. They identified the lowest lying excitations as single *d–d* ligand field excitations, followed by double *d–d* excitations, Mn 3*d* to 4*s* excitations, and finally the O 2*p* to Mn 3*d* charge transfer excitations. Alloying with Zn lowered the highest excitation energy but did not significantly impact the lower-energy excitations.

Another application of these embedded correlated wavefunction methods is to study the effect of dopants on excitations in transition metal oxides. Muñoz-García et al. [266, 267] used CASSCF/CASPT2 with an embedded cluster model including AIMPs to understand shifts in excited states of main character Ce $4f^1$, Ce $5d^1$, and Ce $6s^1$ induced by codoping yttrium aluminum garnet ($Y_3Al_5O_{12}$) with Ce and Ga or La. They reproduced the Ce $4f \rightarrow 5d$ blueshift upon codoping with Ga and explained it as a consequence of geometric distortions [266]. They also showed how codoping with La introduces a redshift of the first Ce $4f \rightarrow 5d$, in agreement with experiment, while the second absorption experiences a blueshift [267].

The embedded correlated wavefunction method can also be used to identify surface-specific excitations in materials. Geleijns et al. [268] studied local excitations on the NiO(100) surface, using a cluster model embedded in AIMPs and applying CASSCF/CASPT2 to solve for the wavefunctions of the lowest 15 d^8 states of a Ni^{2+} ion on the surface. They confirmed the existence of surface-specific *d–d* excitations at 0.6 and 2.1 eV, and showed that the lowest local charge transfer state is 2 eV lower than in bulk NiO. Their study also showed the strong influence of the embedding model, as excitations were heavily influenced by using either point charges or AIMPs. Fink [269] studied excitations in the polar O-terminated $ZnO\left(000\overline{1}\right)$ surface with various defects and in bulk ZnO, using a cluster model embedded in a point charge array and CASSCF or a multiconfigurational coupled electron pair approximation [270]. She found that the oxygen vacancy in bulk ZnO is characterized by absorption at 3.19 eV, in agreement with experiment, whereas the corresponding surface excitation is more than 0.5 eV higher in energy. These excitations are well above the optical band gap of ZnO, explaining why these transitions cannot be observed experimentally.

This level of theory can also help to interpret XPS spectra by solving for the wavefunctions of ionized clusters to create core-holes. Hozoi et al. [271] used nonorthogonal CI with an NiO cluster embedded in a point charge array to interpret the 3*s* XPS spectrum. They found good agreement with experiment, and described each state in terms of a few key configurations. Bagus and Ilton [272] also explained the XPS spectrum in MnO using Dirac relativistic CI and a cluster model embedded in a point charge environment.

4.3 Quantum Mechanical Embedding

The purely electrostatic representation in electrostatic embedding can be insufficient to describe cluster-environment coupling in materials whose bonding character is not purely ionic. To model these materials, the embedding potential must incorporate non-classical interactions. A formal theory of embedding that accounted for non-classical interactions was first developed by Grimley and Pisani [273], with an early solution scheme that was based on Green's function techniques. Gunnarsson et al. [274, 275] generalized Grimley and Pisani's methods, and derived a Kohn–Sham scheme that confined the solution to a set of localized functions. Pisani et al. [276–279] extended this perturbed crystal approach based on the one-electron Green's function method, where the one-electron Green's function in the defect region is evaluated within perturbation theory using the Green's function of the unperturbed host as a reference and a perturbing potential localized within the embedded region. Inglesfield developed a related approach that constructs an embedding potential from the Green's function of a bulk crystal to use in calculations of surfaces [280]. Scheffler et al. proposed a similar Green's function–based method to describe localized perturbations such as isolated adsorbates on crystal surfaces [281].

A different approach for correlated wavefunction embedding was proposed by Whitten and coworkers, who developed orbital space partitioning for embedded CI [282–284]. Orbital space partitioning models the electron density of the environment using an orbital subspace that then interacts with the orbital subspace of the QM cluster. Orbital space partitioning as proposed by Whitten et al. typically begins with a single-determinant wavefunction (i.e., HF) solution for a large cluster, which can be subdivided into the region of interest and the background. The one-electron orbitals from the single reference wavefunction are then partitioned into a subspace localized on the region of interest and a complementary subspace localized on the environment. A number of localization procedures have been proposed [285]. The localized orbitals in the environment subspace are used to construct effective Coulomb and exchange operators [286, 287], which act upon the quantum cluster within the CI calculation. Boundary potentials are also derived by analyzing penetration of the environment orbitals within the embedded cluster. The basis set for the embedded cluster is then augmented, and a CI calculation is performed using the localized orbital subspace of the quantum cluster. Stoll and

coworkers [288, 289] proposed a similar cluster-in-solid embedding technique that extracts its effective one-electron Coulomb and exchange operators from a periodic HF calculation, such that the subsequent correlation calculations are subject to an infinite frozen HF environment. These models account for the electrons in the environment in an approximate way, but in a still more sophisticated manner than the electrostatic model.

The scheme for orbital space partitioning assumes that the one-electron orbitals can be localized, but a localized description of bonding is not always appropriate, such as in metals. In such cases, it is impractical to partition the electron density using localized orbitals; instead, the electron density can be partitioned via charge densities alone, thus avoiding the localization procedure. This approach is known as density-based embedding, where the total system density ρ_{tot} is partitioned into a density associated with the embedded cluster, ρ_{I}, and a density associated with the background, ρ_{II}, whose densities must sum to the total system density:

$$\rho_{\text{I}} + \rho_{\text{II}} = \rho_{\text{tot}} \tag{23}$$

The coupling between the background and cluster densities is accounted for by an effective, one-electron potential V_{emb} that is introduced into the Hamiltonian (shown here to represent KS-DFT) applied to the region of interest:

$$\left(-\frac{\nabla^2}{2} + V_{\text{s}}[\rho_{\text{I}}](\mathbf{r}) + V_{\text{emb}}[\rho_{\text{tot}}, \rho_{\text{I}}](\mathbf{r})\right)\psi_{\text{I},i}(\mathbf{r}) = \epsilon_{\mathbf{i}}\psi_{\text{I},i}(\mathbf{r}) \tag{24}$$

where V_{s} is the typical KS potential for the isolated embedded cluster. This approach is rooted in the subsystem formulation of DFT by Cortona [290], whose strategy was to embed a DFT calculation within an orbital-free DFT background, thereby reducing a periodic DFT calculation to that of a single atom. Wesolowski and Warshel built on Cortona's work by introducing the frozen-density embedding scheme [291], which partitions the total density into the density of an active subsystem and a frozen environment, and where the effect of the frozen environment is accounted for by an effective embedding potential based on DFT. Density-based partitioning was extended further by Carter and coworkers [292–298] to go beyond DFT in DFT embedding to embed a correlated wavefunction calculation using a DFT-based embedding potential for the effect of the environment.

There are a number of methods to model the subsystem-environment interaction. One approach is to use a model DFT functional to represent the interaction energy, as first proposed by Cortona [290]. The embedding potential includes cluster/background coupling from kinetic, Hartree, and exchange-correlation contributions:

$$\begin{aligned} V_{\text{emb}}[\rho_{\text{tot}}, \rho_{\text{I}}](\mathbf{r}) = {} & V_{T_{\text{s}}}[\rho_{\text{tot}}, \rho_{\text{I}}](\mathbf{r}) + V_J[\rho_{\text{tot}}, \rho_{\text{I}}](\mathbf{r}) + V_{\text{xc}}[\rho_{\text{tot}}, \rho_{\text{I}}](\mathbf{r}) \\ & + V_{\text{ion}}^{\text{tot}}(\mathbf{r}) - V_{\text{ion}}^{\text{I}}(\mathbf{r}) \end{aligned} \tag{25}$$

where the potential due to ions in the environment are accounted for by $V_{\text{ion}}^{\text{tot}}(\mathbf{r}) - V_{\text{ion}}^{\text{I}}(\mathbf{r})$, the kinetic potential is

$$V_{T_s}[\rho_{\text{tot}}, \rho_{\text{I}}](\mathbf{r}) = \frac{\delta T_s[\rho_{\text{tot}}]}{\delta \rho_{\text{tot}}(\mathbf{r})} - \frac{\delta T_s[\rho_{\text{I}}]}{\delta \rho_{\text{I}}(\mathbf{r})}, \tag{26}$$

the Hartree potential is

$$V_J[\rho_{\text{tot}}, \rho_{\text{I}}](\mathbf{r}) = \frac{\delta J[\rho_{\text{tot}}]}{\delta \rho_{\text{tot}}(\mathbf{r})} - \frac{\delta J[\rho_{\text{I}}]}{\delta \rho_{\text{I}}(\mathbf{r})}, \tag{27}$$

and the exchange-correlation potential is

$$V_{\text{xc}}[\rho_{\text{tot}}, \rho_{\text{I}}](\mathbf{r}) = \frac{\delta E_{\text{xc}}[\rho_{\text{tot}}]}{\delta \rho_{\text{tot}}(\mathbf{r})} - \frac{\delta E_{\text{xc}}[\rho_{\text{I}}]}{\delta \rho_{\text{I}}(\mathbf{r})}. \tag{28}$$

While the Hartree and exchange-correlation contributions to coupling can be easily modeled at the KS-DFT level using standard exchange-correlation functionals, the kinetic energy contribution is more difficult to model. This is because standard KS-DFT calculates the kinetic energy using an orbital-based formulation, and with density-based partitioning there is no orbital representation of the background. Even within an orbital partitioning scheme, the orbital subspaces in the two regions are not necessarily orthogonal to each other, resulting in a non-additive kinetic energy term that must be approximated. The kinetic energy potential typically has been approximated using an orbital-free DFT functional. Cortona modeled the kinetic energy in the cluster/background coupling using the Thomas–Fermi kinetic energy density functional that is exact for the homogeneous electron gas [299, 300]. Other common approximations for the kinetic energy density functional include the von Weizsäcker result for the limit of a one-orbital density [301], the Wang–Teter functional [302], and the Wang–Govind–Carter [303, 304] functionals, among others. The non-additive kinetic energy can also be computed exactly with OEP methods. Goodpaster et al. [305, 306] proposed a formally exact protocol that uses a Levy constrained search [307] as implemented by Zhao, Morrison, and Parr [308–310] to obtain first a full set of KS orbitals for the total density, after which the non-additive kinetic energy is calculated exactly using the total and subsystem orbital sets via the approach by King and Handy [311]. Fux et al. [312] proposed another scheme using the OEP method of Wu and Yang [313] to reconstruct the KS potential for the embedded subsystem, which is then subsequently used to define an accurate non-additive kinetic energy potential.

To eschew the problems with approximate kinetic-energy density functionals within the model DFT potential, several methods derive numerical embedding potentials that completely replace the entire density functional potential, where these new potentials are derived via an inversion technique from the partitioned reference density. Roncero et al. [314] first introduced such a scheme, where the density partitioning is first fixed and the embedding potential is subsequently derived. They later improved this scheme by optimizing the embedding potential and the density partitioning within the same iterative procedure, although there is

no guarantee of their uniqueness [315]. Huang et al. [316] proposed a scheme where density partitioning and the embedding potential are ensured to be unique by constraining the embedding potential to be the same for the cluster and environment. Here, the embedding potential is solved for via an extension of the OEP method. This scheme is closely related to partition density functional theory, as proposed by Cohen and coworkers [317–321]. These methods differ in that partition density functional theory allows for fractional numbers of electrons in the partitioned subsystem densities, while Huang et al. constrain the electron number in each subsystem to be an integer so as to allow correlated wavefunction calculations to be performed, which require this constraint. While Huang et al. derived a partitioning scheme and embedding potential that is dependent only on the reference density from a DFT calculation, a self-consistent scheme was proposed that updates the partitioning and embedding potential iteratively using contributions of the new density from the correlated wavefunction method. Huang and Carter [322] later reformulated this density-based embedding theory in terms of functionals of the embedding potential, thereby straightforwardly enforcing the constraint that all subsystems share a common embedding potential. Huang and Carter also introduced an alternative to Wu and Yang's more expensive formalism for the OEP calculation by reformulating the potential functional derivative with respect to the total energy in terms of finite differences, thereby improving the efficiency of OEP calculations [49].

Another approach is to avoid the computational expense of OEP methods and the approximations in orbital-free expressions for the kinetic energy altogether. Manby et al. [323] devised a scheme to entirely remove the contribution of the non-additive kinetic energy. They do so by exploiting the fact that if the subsystem densities are constructed from mutually orthogonal orbitals, the kinetic energy of the entire system is simply the sum of the kinetic energies of the isolated subsystems, with no non-additive contribution. They therefore enforce mutual orthogonality between subsystem orbitals through the use of a level shifting projection operator, thereby eliminating the non-additive kinetic energy term. Dependence on the level shifting operator is eliminated through perturbation theory. While mutual orthogonality has been employed in orbital-space partitioning methods for decades, it had not been used before to construct a formally exact DFT embedding scheme.

Most of these state-of-the-art density-based embedding schemes have been applied thus far to molecules [306, 315, 323, 324] or to localized impurities/adsorption at metal surfaces (e.g., Kondo systems [325–327], electron-transfer-induced dissociation [328, 329]) and have not yet been used to treat any extended transition metal oxides. Consequently, it is difficult to evaluate the advantages and disadvantages of these methods with respect to modeling more complex materials like transition metal oxides. However, DFT-based embedding potentials were compared recently to point-charge embedding in modeling the low-lying optical excitations of MgO, selected as a prototype for metal oxides [253]. There, the density functional embedding model resulted in a significantly underestimated optical gap (5.63 eV) in comparison to experiment (7.5–7.8 [330, 331]), while the

point charge embedded prediction of 6.8 eV was much closer. Overall, the (inexpensive) embedded cluster model showed reduced accuracy in comparison to (expensive) *GW*/BSE predictions (7.2–7.7 eV [192, 332, 333]), unfortunately indicating that embedded clusters are not the most appropriate model for excitations involving delocalized electrons like the exciton in MgO. While this identifies a weakness in the density-based embedding model to describe delocalized excitations, based on the prior success of point charge embedding with transition metal oxides, the density-based models may still be promising in studying the more localized excited states present in such materials, especially for transition metal oxides with a larger degree of covalency. Indeed, the related cluster-in-solid embedding technique of Birkenheuer et al. [288, 289] has been applied by Hozoi et al. [334] to study the d-level splitting in layered cuprates, where the correlated cluster was modeled with CASSCF/MRSDCI. The d-level splitting was in excellent agreement with resonant inelastic X-ray scattering (RIXS) measurements.

5 Conclusions

As we have reviewed, a wide range of theoretical methods is available to calculate the band structures and optical properties of transition metal oxides. No single method can be declared as the universal approach to calculate all types of electronic excitation spectra, as varying models are suitable for describing differing types of excitations. *GW* best models charged excitations that can be appropriately described within a delocalized band picture, while the related BSE and TD-DFT can help to explain absorption spectra derived from band-to-band excitations. However, for localized, neutral excitations, embedded correlated wavefunction methods may best capture the essential physics. Within each of these parent theories are a number of implementations that each rely on some form of approximation, such that no one of these methods performs predominantly best in describing excitations in transition metal oxides.

The progress in each of these fields continues to be significant, and the future promises even greater advances. *GW* has already evolved considerably from its roots as a single perturbation on an LDA reference. As *GW* continues to advance, its more modern implementations (such as those with greater self-consistency) need to be better evaluated in the context of their application to transition metal oxides, to better identify the source of their deficiencies. While we may hope to develop a universal *GW* approach that is accurate for all materials, based on the observed variability in accuracy within each method, it is likely that the current dependence on identifying a material-specific optimal approach will persist.

Similarly, the field of embedded correlated wavefunction theory has made great strides in the past few decades. However, a survey of the literature reveals that the application of these methods to transition metal oxides has not entirely kept abreast. A more thorough evaluation of these approaches is needed to assess their ability to model excitations in these more complex materials, and specifically to judge whether

density-based embedding potentials actually represent the cluster-background coupling in these systems better than electrostatic embedding.

Regardless of an enduring inability to achieve all-encompassing accuracy within a single method, it is clear that each individual theory will continue to improve in accuracy and efficiency, broadening the bounds of its capability to describe larger or more complex materials and phenomena. These advances will surely be coupled with greater understanding of material properties and improved materials design for numerous optical and optoelectronic applications.

Acknowledgments We are grateful to the U.S. Air Force Office of Scientific Research and the U.S. Department of Energy, Basic Energy Sciences for support of our research in this area.

References

1. Carter EA (2008) Challenges in modeling materials properties without experimental input. Science 321:800–803
2. Hohenberg P, Kohn W (1964) Inhomogeneous electron gas. Phys Rev 136:B864–B871
3. Kohn W, Sham LJ (1965) Self-consistent equations including exchange and correlation effects. Phys Rev 140:A1133–A1138
4. Bowler DR, Miyazaki T, Gillan MJ (2002) Recent progress in linear scaling ab initio electronic structure techniques. J Phys Condens Matter 14:2781
5. Ceperley DM, Alder BJ (1980) Ground state of the electron gas by a stochastic method. Phys Rev Lett 45:566–569
6. Vosko SH, Wilk L, Nusair M (1980) Accurate spin-dependent electron liquid correlation energies for local spin density calculations: a critical analysis. Can J Phys 58:1200–1211
7. Perdew JP, Zunger A (1981) Self-interaction correction to density-functional approximations for many-electron systems. Phys Rev B 23:5048–5079
8. Perdew JP, Wang Y (1992) Accurate and simple analytic representation of the electron-gas correlation energy. Phys Rev B 45:13244–13249
9. Perdew JP, Chevary JA, Vosko SH, Jackson KA, Pederson MR, Singh DJ, Fiolhais C (1992) Atoms, molecules, solids, and surfaces: applications of the generalized gradient approximation for exchange and correlation. Phys Rev B 46:6671–6687
10. Perdew JP, Burke K, Ernzerhof M (1996) Generalized gradient approximation made simple. Phys Rev Lett 77:3865–3868
11. Perdew JP, Burke K, Ernzerhof M (1997) Generalized gradient approximation made simple [Phys Rev Lett 77:3865 (1996)]. Phys Rev Lett 78:1396
12. Perdew JP, Burke K, Ernzerhof M (1998) Perdew, Burke, and Ernzerhof reply. Phys Rev Lett 80:891
13. Zhang Y, Yang W (1998) Comment on "Generalized gradient approximation made simple". Phys Rev Lett 80:890
14. Hammer B, Hansen LB, Nørskov JK (1999) Improved adsorption energetics within density-functional theory using revised Perdew–Burke–Ernzerhof functionals. Phys Rev B 59: 7413–7421
15. Anisimov VI, Zaanen J, Andersen OK (1991) Band theory and Mott insulators: Hubbard U instead of Stoner I. Phys Rev B 44:943–954
16. Anisimov VI, Solovyev IV, Korotin MA, Czyżyk MT, Sawatzky GA (1993) Density-functional theory and NiO photoemission spectra. Phys Rev B 48:16929–16934

17. Solovyev IV, Dederichs PH, Anisimov VI (1994) Corrected atomic limit in the local-density approximation and the electronic structure of d impurities in Rb. Phys Rev B 50: 16861–16871
18. Czyzyk MT, Sawatzky GA (1994) Local-density functional and on-site correlations: the electronic structure of La_2CuO_4 and $LaCuO_3$. Phys Rev B 49:14211–14228
19. Liechtenstein AI, Anisimov VI, Zaanen J (1995) Density-functional theory and strong interactions: orbital ordering in Mott–Hubbard insulators. Phys Rev B 52:R5467–R5470
20. Anisimov VI, Aryasetiawan F, Lichtenstein AI (1997) First-principles calculations of the electronic structure and spectra of strongly correlated systems: the LDA+U method. J Phys Condens Matter 9:767–808
21. Dudarev SL, Liechtenstein AI, Castell MR, Briggs GAD, Sutton AP (1997) Surface states on NiO (100) and the origin of the contrast reversal in atomically resolved scanning tunneling microscope images. Phys Rev B 56:4900–4908
22. Dudarev SL, Botton GA, Savrasov SY, Humphreys CJ, Sutton AP (1998) Electron-energy-loss spectra and the structural stability of nickel oxide: an LSDA+U study. Phys Rev B 57: 1505–1509
23. Anisimov VI, Gunnarsson O (1991) Density-functional calculation of effective Coulomb interactions in metals. Phys Rev B 43:7570–7574
24. Gunnarsson O, Andersen OK, Jepsen O, Zaanen J (1989) Density-functional calculation of the parameters in the Anderson model: application to Mn in CdTe. Phys Rev B 39:1708–1722
25. Cococcioni M, de Gironcoli S (2005) Linear response approach to the calculation of the effective interaction parameters in the LDA+U method. Phys Rev B 71:035105 (16 pp)
26. Springer M, Aryasetiawan F (1998) Frequency-dependent screened interaction in Ni within the random-phase approximation. Phys Rev B 57:4364–4368
27. Kotani T (2000) Ab initio random-phase-approximation calculation of the frequency-dependent effective interaction between 3d electrons: Ni, Fe, and MnO. J Phys Condens Matter 12:2413–2422
28. Aryasetiawan F, Imada M, Georges A, Kotliar G, Biermann S, Lichtenstein AI (2004) Frequency-dependent local interactions and low-energy effective models from electronic structure calculations. Phys Rev B 70:195104 (8 pp)
29. Aryasetiawan F, Karlsson K, Jepsen O, Schönberger U (2006) Calculations of Hubbard U from first-principles. Phys Rev B 74:125106 (8 pp)
30. Kulik HJ, Cococcioni M, Scherlis DA, Marzari N (2006) Density functional theory in transition-metal chemistry: a self-consistent Hubbard U approach. Phys Rev Lett 97: 103001 (4 pp)
31. Kulik HJ, Marzari N (2008) A self-consistent Hubbard U density-functional theory approach to the addition-elimination reactions of hydrocarbons on bare FeO^+. J Chem Phys 129: 134314 (12 pp)
32. Kulik HJ, Marzari N (2010) Systematic study of first-row transition-metal diatomic molecules: a self-consistent DFT+U approach. J Chem Phys 133:114103 (16 pp)
33. Shih B-C, Zhang Y, Zhang W, Zhang P (2012) Screened Coulomb interaction of localized electrons in solids from first principles. Phys Rev B 85:045132 (9 pp)
34. Mosey NJ, Carter EA (2007) Ab initio evaluation of Coulomb and exchange parameters for DFT+U calculations. Phys Rev B 76:155123 (13 pp)
35. Mosey NJ, Liao P, Carter EA (2008) Rotationally invariant ab initio evaluation of Coulomb and exchange parameters for DFT+U calculations. J Chem Phys 129:014103 (13 pp)
36. Kioupakis E, Zhang P, Cohen ML, Louie SG (2008) GW quasiparticle corrections to the LDA+U/GGA+U electronic structure of bcc hydrogen. Phys Rev B 77:155114 (4 pp)
37. Krieger JB, Li Y, Iafrate GJ (1992) Construction and application of an accurate local spin-polarized Kohn–Sham potential with integer discontinuity: exchange-only theory. Phys Rev 45:101–126
38. Sharp RT, Horton GK (1953) A variational approach to the unipotential many-electron problem. Phys Rev 90:317

39. Rose JH Jr, Shore HB (1975) Calculation method for the inhomogeneous electron gas. Solid State Commun 17:327–330
40. Talman JD, Shadwick WF (1976) Optimized effective atomic central potential. Phys Rev 14:36–40
41. Krieger JB, Li Y, Iafrate GJ (1992) Systematic approximations to the optimized effective potential: application to orbital-density-functional theory. Phys Rev 46:5453–5458
42. Bulgac A, Lewenkopf C, Mickrjukov V (1995) Generalized local approximation to the exchange potential. Phys Rev B 52:16476–16485
43. Gonze X (1996) Towards a potential-based conjugate gradient algorithm for order-N self-consistent total energy calculations. Phys Rev B 54:4383–4386
44. Fritsche L, Yuan J (1998) Alternative approach to the optimized effective potential method. Phys Rev 57:3425–3432
45. Hyman RA, Stiles MD, Zangwill A (2000) Gradient search method for orbital-dependent density-functional calculations. Phys Rev B 62:15521–15526
46. Hirata S, Ivanov S, Grabowski I, Bartlett RJ, Burke K, Talman JD (2001) Can optimized effective potentials be determined uniquely? J Chem Phys 115:1635–1649
47. Yang W, Wu Q (2002) Direct method for optimized effective potentials in density-functional theory. Phys Rev Lett 89:143002 (4 pp)
48. Kümmel S, Perdew JP (2003) Simple iterative construction of the optimized effective potential for orbital functionals, including exact exchange. Phys Rev Lett 90:043004 (4 pp)
49. Huang C, Carter EA (2011) Direct minimization of the optimized effective problem based on efficient finite differences. Phys Rev B 84:165122 (6 pp)
50. Becke AD (1993) A new mixing of Hartree–Fock and local density-functional theories. J Chem Phys 98:1372–1377
51. Adamo C, Barone V (1999) Toward reliable density functional methods without adjustable parameters: the PBE0 model. J Chem Phys 110:6158–6170
52. Perdew JP, Ernzerhof M, Burke K (1996) Rationale for mixing exact exchange with density functional approximations. J Chem Phys 105:9982–9985
53. Savin A (1995) Beyond the Kohn–Sham determinant. In: Chong DP (ed) Recent Advances in Computational Chemistry. World Scientific Publishing, Singapore, pp 129–153
54. Leininger T, Stoll H, Werner H-J, Savin A (1997) Combining long-range configuration interaction with short-range density functionals. Chem Phys Lett 275:151–160
55. Savin A, Flad H-J (1995) Density functionals for the Yukawa electron–electron interaction. Int J Quantum Chem 56:327–332
56. Iikura H, Tsuneda T, Yanai T, Hirao K (2001) A long-range correction scheme for generalized-gradient-approximation exchange functionals. J Chem Phys 115:3540–3544
57. Vydrov OA, Scuseria GE (2006) Assessment of a long-range corrected hybrid functional. J Chem Phys 125:234109 (9 pp)
58. Cohen AJ, Mori-Sánchez P, Yang W (2007) Development of exchange-correlation functionals with minimal many-electron self-interaction error. J Chem Phys 126:191109 (5 pp)
59. Chai J-D, Head-Gordon M (2008) Systematic optimization of long-range corrected hybrid density functionals. J Chem Phys 128:084106 (15 pp)
60. Chai J-D, Head-Gordon M (2008) Long-range corrected hybrid density functionals with damped atom–atom dispersion corrections. Phys Chem Chem Phys 10:6615–6620
61. Rohrdanz MA, Martins KM, Herbert JM (2009) A long-range-corrected density functional that performs well for both ground-state properties and time-dependent density functional theory excitation energies, including charge-transfer excited states. J Chem Phys 130:054112 (8 pp)
62. Heyd J, Scuseria GE, Ernzerhof M (2003) Hybrid functionals based on a screened Coulomb potential. J Chem Phys 118:8207–8215
63. Heyd J, Scuseria GE (2004) Assessment and validation of a screened Coulomb hybrid density functional. J Chem Phys 120:7274–7280

64. Heyd J, Scuseria GE (2004) Efficient hybrid density functional calculations in solids: assessment of the Heyd–Scuseria–Ernzerhof screened Coulomb hybrid functional. J Chem Phys 121:1187–1192
65. Heyd J, Peralta JE, Scuseria GE, Martin RL (2005) Energy band gaps and lattice parameters evaluated with the Heyd-Scuseria-Ernzerhof screened hybrid functional. J Chem Phys 123: 174101 (8 pp)
66. Becke AD (1993) Density-functional thermochemistry. III. The role of exact exchange. J Chem Phys 98:5648–5652
67. Lee C, Yang W, Parr RG (1988) Development of the Colle-Salvetti correlation-energy formula into a functional of the electron density. Phys Rev B 37:785–789
68. Stephens PJ, Devlin FJ, Chabalowski CF, Frisch MJ (1994) Ab initio calculation of vibrational absorption and circular dichroism spectra using density functional force fields. J Phys Chem 98:11623–11627
69. Perdew JP, Parr RG, Levy M, Balduz JL (1982) Density-functional theory for fractional particle number: derivative discontinuities of the energy. Phys Rev Lett 49:1691–1694
70. Almbladh C-O, von Barth U (1985) Exact results for the charge and spin densities, exchange-correlation potentials, and density-functional eigenvalues. Phys Rev B 31:3231–3244
71. Perdew JP, Levy M (1997) Comment on "Significance of the highest occupied Kohn–Sham eigenvalue". Phys Rev B 56:16021–16028
72. Sham LJ, Schlüter M (1983) Density-functional theory of the energy gap. Phys Rev Lett 51: 1888–1891
73. Perdew JP, Levy M (1983) Physical content of the exact Kohn–Sham orbital energies: band gaps and derivative discontinuities. Phys Rev Lett 51:1884–1887
74. Chan MKY, Ceder G (2010) Efficient band gap prediction for solids. Phys Rev Lett 105: 196403–196406
75. Leslie M, Gillan NJ (1985) The energy and elastic dipole tensor of defects in ionic crystals calculated by the supercell method. J Phys C Solid State Phys 18:973–982
76. Makov G, Payne MC (1995) Periodic boundary conditions in ab initio calculations. Phys Rev B 51:4014–4022
77. Schultz PA (1999) Local electrostatic moments and periodic boundary conditions. Phys Rev B 60:1551–1554
78. Schultz PA (2000) Charged local defects in extended systems. Phys Rev Lett 84:1942–1945
79. Özgür Ü, Alivov YI, Liu C, Teke A, Reshchikov MA, Doğan S, Avrutin V, Cho S-J, Morkoç H (2005) A comprehensive review of ZnO materials and devices. J Appl Phys 98:041301 (103 pp)
80. Stein T, Autschbach J, Govind N, Kronik L, Baer R (2012) Curvature and frontier orbital energies in density functional theory. J Phys Chem Lett 3:3740–3744
81. Seidl A, Görling A, Vogl P, Majewski JA, Levy M (1996) Generalized Kohn–Sham schemes and the band-gap problem. Phys Rev B 53:3764–3774
82. Kronik L, Stein T, Refaely-Abramson S, Baer R (2012) Excitation gaps of finite-sized systems from optimally tuned range-separated hybrid functionals. J Chem Theory Comput 8:1515–1531
83. Baer R, Neuhauser D (2005) Density functional theory with correct long-range asymptotic behavior. Phys Rev Lett 94:043002 (4 pp)
84. Livshits E, Baer R (2007) A well-tempered density functional theory of electrons in molecules. Phys Chem Chem Phys 9:2932–2941
85. Salzner U, Baer R (2009) Koopmans' springs to life. J Chem Phys 131:231101 (4 pp)
86. Refaely-Abramson S, Baer R, Kronik L (2011) Fundamental and excitation gaps in molecules of relevance for organic photovoltaics from an optimally tuned range-separated hybrid functional. Phys Rev B 84:075144 (8 pp)
87. Refaely-Abramson S, Sharifzadeh S, Govind N, Autschbach J, Neaton JB, Baer R, Kronik L (2012) Quasiparticle spectra from a nonempirical optimally tuned range-separated hybrid density functional. Phys Rev Lett 109:226405

88. Eisenberg HR, Baer R (2009) A new generalized Kohn–Sham method for fundamental band-gaps in solids. Phys Chem Chem Phys 11:4674–4680
89. Runge E, Gross EKU (1984) Density-functional theory for time-dependent systems. Phys Rev Lett 52:997–1000
90. Petersilka M, Gossmann UJ, Gross EKU (1996) Excitation energies from time-dependent density-functional theory. Phys Rev Lett 76:1212–1215
91. Casida ME (1996) Time-dependent density functional response theory of molecular systems: theory, computational methods, and functionals. In: Seminario JM (ed) Theor Comput Chem. Elsevier, Amsterdam, pp 391–439
92. Chelikowsky JR, Kronik L, Vasiliev I (2003) Time-dependent density-functional calculations for the optical spectra of molecules, clusters, and nanocrystals. J Phys Condens Matter 15: R1517–R1547
93. Burke K, Werschnik J, Gross EKU (2005) Time-dependent density functional theory: past, present, and future. J Chem Phys 123:062206 (9 pp)
94. Sottile F, Bruneval F, Marinopoulos AG, Dash LK, Botti S, Olevano V, Vast N, Rubio A, Reining L (2005) TDDFT from molecules to solids: the role of long-range interactions. Int J Quantum Chem 102:684–701
95. Botti S, Schindlmayr A, Sole RD, Reining L (2007) Time-dependent density-functional theory for extended systems. Rep Prog Phys 70:357–407
96. Elliott P, Furche F, Burke K (2009) Excited states from time-dependent density functional theory. In: Lipkowitz KB, Cundari TR (eds) Rev Comput Chem. Wiley, Hoboken, pp 91–165
97. Marques MA, Maitra NT, Nogueira FM, Gross EKU, Rubio A (2012) Fundamentals of time-dependent density functional theory. Springer, Berlin
98. Onida G, Reining L, Rubio A (2002) Electronic excitations: density-functional versus many-body Green's-function approaches. Rev Mod Phys 74:601–659
99. Sottile F, Olevano V, Reining L (2003) Parameter-free calculation of response functions in time-dependent density-functional theory. Phys Rev Lett 91:056402 (4 pp)
100. Rocca D, Gebauer R, Saad Y, Baroni S (2008) Turbo charging time-dependent density-functional theory with Lanczos chains. J Chem Phys 128:154105 (14 pp)
101. Malcıoğlu OB, Gebauer R, Rocca D, Baroni S (2011) turboTDDFT – a code for the simulation of molecular spectra using the Liouville–Lanczos approach to time-dependent density-functional perturbation theory. Comput Phys Commun 182:1744–1754
102. De Angelis F, Armelao L (2010) Optical properties of ZnO nanostructures: a hybrid DFT/TDDFT investigation. Phys Chem Chem Phys 13:467–475
103. Monticone S, Tufeu R, Kanaev AV (1998) Complex nature of the UV and visible fluorescence of colloidal ZnO nanoparticles. J Phys Chem B 102:2854–2862
104. Malloci G, Chiodo L, Rubio A, Mattoni A (2012) Structural and optoelectronic properties of unsaturated ZnO and ZnS nanoclusters. J Phys Chem C 116:8741–8746
105. De Angelis F, Fantacci S, Selloni A (2008) Alignment of the dye's molecular levels with the TiO_2 band edges in dye-sensitized solar cells: a DFT–TDDFT study. Nanotechnology 19: 424002 (7 pp)
106. Suzuki S, Tsuneda T, Hirao K (2012) A theoretical investigation on photocatalytic oxidation on the TiO_2 surface. J Chem Phys 136:024706 (6 pp)
107. Becke AD (1988) Density-functional exchange-energy approximation with correct asymptotic behavior. Phys Rev 38:3098–3100
108. Nakamura I, Negishi N, Kutsuna S, Ihara T, Sugihara S, Takeuchi K (2000) Role of oxygen vacancy in the plasma-treated TiO_2 photocatalyst with visible light activity for NO removal. J Mol Catal Chem 161:205–212
109. Breckenridge RG, Hosler WR (1953) Electrical properties of titanium dioxide semiconductors. Phys Rev 91:793–802
110. Govind N, Lopata K, Rousseau R, Andersen A, Kowalski K (2011) Visible light absorption of N-doped TiO_2 rutile using (LR/RT)-TDDFT and active space EOMCCSD calculations. J Phys Chem Lett 2:2696–2701

111. Chambers SA, Cheung SH, Shutthanandan V, Thevuthasan S, Bowman MK, Joly AG (2007) Properties of structurally excellent N-doped TiO_2 rutile. Chem Phys 339:27–35
112. Cheung SH, Nachimuthu P, Joly AG, Engelhard MH, Bowman MK, Chambers SA (2007) N incorporation and electronic structure in N-doped TiO_2(1 1 0) rutile. Surf Sci 601:1754–1762
113. Lee C-C, Hsueh HC, Ku W (2010) Dynamical linear response of TDDFT with LDA+U functional: strongly hybridized Frenkel excitons in NiO. Phys Rev B 82:081106 (4 pp)
114. Larson BC, Ku W, Tischler JZ, Lee C-C, Restrepo OD, Eguiluz AG, Zschack P, Finkelstein KD (2007) Nonresonant inelastic X-ray scattering and energy-resolved Wannier function investigation of d-d excitations in NiO and CoO. Phys Rev Lett 99:026401 (4 pp)
115. Müller F, Hüfner S (2008) Angle-resolved electron energy-loss spectroscopy investigation of crystal-field transitions on MnO and NiO surfaces: exchange scattering versus direct scattering. Phys Rev B 78:085438 (7 pp)
116. Hedin L, Lundqvist S (1970) Effects of electron–electron and electron–phonon interactions on the one-electron states of solids. In: Frederick Seitz DT, Ehrenreich H (eds) Solid State Phys. Academic, New York, pp 1–181
117. Hedin L (1965) New method for calculating the one-particle Green's function with application to the electron-gas problem. Phys Rev 139:A796–A823
118. Hybertsen MS, Louie SG (1987) Theory and calculation of quasiparticle energies and band gaps. Comments Condens Matter Phys 13:223–247
119. Gatti M, Bruneval F, Olevano V, Reining L (2007) Understanding correlations in vanadium dioxide from first principles. Phys Rev Lett 99:266402 (4 pp)
120. Aryasetiawan F, Gunnarsson O (1995) Electronic structure of NiO in the GW approximation. Phys Rev Lett 74:3221–3224
121. Van Schilfgaarde M, Kotani T, Faleev SV (2006) Adequacy of approximations in GW theory. Phys Rev B 74:245125 (16 pp)
122. Hüfner S (1985) Mott insulation in transition metal compounds. Z Für Phys B Condens Matter 61:135–138
123. Hüfner S (1985) Hybridization and electron interaction in nickel compounds. Solid State Commun 53:707–710
124. Hüfner S, Osterwalder J, Riesterer T, Hulliger F (1984) Photoemission and inverse photoemission spectroscopy of NiO. Solid State Commun 52:793–796
125. Hüfner S, Hulliger F, Osterwalder J, Riesterer T (1984) On the interpretation of valence band photoemission spectra of NiO. Solid State Commun 50:83–86
126. Hüfner S (1984) Bandstructure and atomic energy levels in Ce-Metal, NiO and NiS. Z Für Phys B Condens Matter 58:1–6
127. Hüfner S, Steiner P, Sander I, Neumann M, Witzel S (1991) Photoemission on NiO. Z Für Phys B Condens Matter 83:185–192
128. Fujimori A, Minami F, Sugano S (1984) Multielectron satellites and spin polarization in photoemission from Ni compounds. Phys Rev B 29:5225–5227
129. Fujimori A, Minami F (1984) Valence-band photoemission and optical absorption in nickel compounds. Phys Rev B 30:957–971
130. Oh S-J, Allen JW, Lindau I, Mikkelsen JC (1982) Resonant valence-band satellites and polar fluctuations in nickel and its compounds. Phys Rev B 26:4845–4856
131. Thuler MR, Benbow RL, Hurych Z (1983) Photoemission intensities at the 3p threshold resonance of NiO and Ni. Phys Rev B 27:2082–2088
132. Davis LC (1986) Photoemission from transition metals and their compounds. J Appl Phys 59:R25–R64
133. Shen Z-X, List RS, Dessau DS et al (1991) Electronic structure of NiO: correlation and band effects. Phys Rev B 44:3604–3626
134. Bruneval F, Vast N, Reining L, Izquierdo M, Sirotti F, Barrett N (2006) Exchange and correlation effects in electronic excitations of Cu_2O. Phys Rev Lett 97:267601 (4 pp)
135. Kang W, Hybertsen MS (2010) Quasiparticle and optical properties of rutile and anatase TiO_2. Phys Rev B 82:085203 (11 pp)

136. Tezuka Y, Shin S, Ishii T, Ejima T, Suzuki S, Sato S (1994) Photoemission and Bremsstrahlung isochromat spectroscopy studies of TiO_2 (rutile) and $SrTiO_3$. J Phys Soc Jpn 63:347–357
137. Tang H, Lévy F, Berger H, Schmid PE (1995) Urbach tail of anatase TiO_2. Phys Rev B 52:7771–7774
138. Shin S, Suga S, Taniguchi M, Fujisawa M, Kanzaki H, Fujimori A, Daimon H, Ueda Y, Kosuge K, Kachi S (1990) Vacuum-ultraviolet reflectance and photoemission study of the metal-insulator phase transitions in VO_2, V_6O_{13}, and V_2O_3. Phys Rev B 41:4993–5009
139. Sawatzky GA, Allen JW (1984) Magnitude and origin of the band gap in NiO. Phys Rev Lett 53:2339–2342
140. Brahms S, Nikitine S, Dahl JP (1966) On the band structure and the absorption spectrum of Cu_2O. Phys Lett 22:31–33
141. Koffyberg FP (1976) Thermoreflectance spectra of CdO: band gaps and band-population effects. Phys Rev B 13:4470–4476
142. McGuinness C, Stagarescu CB, Ryan PJ, Downes JE, Fu D, Smith KE, Egdell RG (2003) Influence of shallow core-level hybridization on the electronic structure of post-transition-metal oxides studied using soft X-ray emission and absorption. Phys Rev B 68:165104 (10 pp)
143. Jiang H, Gomez-Abal RI, Rinke P, Scheffler M (2010) Electronic band structure of zirconia and hafnia polymorphs from the GW perspective. Phys Rev B 81:085119 (9 pp)
144. Bersch E, Rangan S, Bartynski RA, Garfunkel E, Vescovo E (2008) Band offsets of ultrathin high-κ oxide films with Si. Phys Rev B 78:085114 (10 pp)
145. Isseroff LY, Carter EA (2012) Importance of reference Hamiltonians containing exact exchange for accurate one-shot GW calculations of Cu_2O. Phys Rev B 85:235142 (7 pp)
146. Shishkin M, Kresse G (2007) Self-consistent GW calculations for semiconductors and insulators. Phys Rev B 75:235102 (9 pp)
147. Liao P, Carter EA (2011) Testing variations of the GW approximation on strongly correlated transition metal oxides: hematite (α-Fe_2O_3) as a benchmark. Phys Chem Chem Phys 13:15189–15199
148. Chiodo L, García-Lastra JM, Iacomino A, Ossicini S, Zhao J, Petek H, Rubio A (2010) Self-energy and excitonic effects in the electronic and optical properties of TiO_2 crystalline phases. Phys Rev B 82:045207 (12 pp)
149. Zimmermann R, Steiner P, Claessen R, Reinert F, Hüfner S, Blaha P, Dufek P (1999) Electronic structure of 3d-transition-metal oxides: on-site Coulomb repulsion versus covalency. J Phys Condens Matter 11:1657–1682
150. Patrick CE, Giustino F (2012) GW quasiparticle bandgaps of anatase TiO_2 starting from DFT+U. J Phys Condens Matter 24:202201 (5 pp)
151. Jiang H, Gomez-Abal RI, Rinke P, Scheffler M (2010) First-principles modeling of localized d states with the GW@LDA+U approach. Phys Rev B 82:045108 (16 pp)
152. Kanan DK, Carter EA (2012) Band gap engineering of MnO via ZnO alloying: a potential new visible-light photocatalyst. J Phys Chem C 116:9876–9887
153. Toroker MC, Kanan DK, Alidoust N, Isseroff LY, Liao P, Carter EA (2011) First principles scheme to evaluate band edge positions in potential transition metal oxide photocatalysts and photoelectrodes. Phys Chem Chem Phys 13:16644–16654
154. Jiang H, Gomez-Abal RI, Rinke P, Scheffler M (2009) Localized and itinerant states in lanthanide oxides united by GW @ LDA+U. Phys Rev Lett 102:126403 (4 pp)
155. Van Elp J, Potze RH, Eskes H, Berger R, Sawatzky GA (1991) Electronic structure of MnO. Phys Rev B 44:1530–1537
156. Kim B, Hong S, Lynch DW (1990) Inverse-photoemission measurement of iron oxides on polycrystalline Fe. Phys Rev B 41:12227–12229
157. Van Elp J, Wieland JL, Eskes H, Kuiper P, Sawatzky GA, de Groot FMF, Turner TS (1991) Electronic structure of CoO, Li-doped CoO, and $LiCoO_2$. Phys Rev B 44:6090–6103
158. Prokofiev AV, Shelykh AI, Melekh BT (1996) Periodicity in the band gap variation of Ln_2X_3 (X = O, S, Se) in the lanthanide series. J Alloys Compd 242:41–44

159. Kimura S, Arai F, Ikezawa M (2000) Optical study on electronic structure of rare-earth sesquioxides. J Phys Soc Jpn 69:3451–3457
160. Zhao Y, Kita K, Kyuno K, Toriumi A (2009) Band gap enhancement and electrical properties of La_2O_3 films doped with Y_2O_3 as high-k gate insulators. Appl Phys Lett 94:042901 (3 pp)
161. Seguini G, Bonera E, Spiga S, Scarel G, Fanciulli M (2004) Energy-band diagram of metal/Lu_2O_3/silicon structures. Appl Phys Lett 85:5316–5318
162. Fuchs F, Furthmüller J, Bechstedt F, Shishkin M, Kresse G (2007) Quasiparticle band structure based on a generalized Kohn–Sham scheme. Phys Rev B 76:115109 (8 pp)
163. Rödl C, Fuchs F, Furthmüller J, Bechstedt F (2009) Quasiparticle band structures of the antiferromagnetic transition-metal oxides MnO, FeO, CoO, and NiO. Phys Rev B 79:235114 (8 pp)
164. Yan Q, Rinke P, Winkelnkemper M, Qteish A, Bimberg D, Scheffler M, Van de Walle CG (2011) Band parameters and strain effects in ZnO and group-III nitrides. Semicond Sci Technol 26:014037 (8 pp)
165. Holm B, von Barth U (1998) Fully self-consistent GW self-energy of the electron gas. Phys Rev B 57:2108–2117
166. Bruneval F, Vast N, Reining L (2006) Effect of self-consistency on quasiparticles in solids. Phys Rev B 74:045102 (15 pp)
167. Gygi F, Baldereschi A (1989) Quasiparticle energies in semiconductors: self-energy correction to the local-density approximation. Phys Rev Lett 62:2160–2163
168. Ye L-H, Asahi R, Peng L-M, Freeman AJ (2012) Model GW study of the late transition metal monoxides. J Chem Phys 137:154110 (7 pp)
169. Massidda S, Continenza A, Posternak M, Baldereschi A (1997) Quasiparticle energy bands of transition-metal oxides within a model GW scheme. Phys Rev B 55:13494–13502
170. Continenza A, Massidda S, Posternak M (1999) Self-energy corrections in VO_2 within a model GW scheme. Phys Rev B 60:15699–15704
171. Massidda S, Resta R, Posternak M, Baldereschi A (1995) Polarization and dynamical charge of ZnO within different one-particle schemes. Phys Rev B 52:R16977–R16980
172. Massidda S, Continenza A, Posternak M, Baldereschi A (1995) Band-structure picture for MnO reexplored: a model GW calculation. Phys Rev Lett 74:2323–2326
173. Park SK, Ishikawa T, Tokura Y (1998) Charge-gap formation upon the Verwey transition in Fe_3O_4. Phys Rev B 58:3717–3720
174. Lany S (2013) Band-structure calculations for the 3d transition metal oxides in GW. Phys Rev B 87:085112 (9 pp)
175. Shin S, Tezuka Y, Kinoshita T, Ishii T, Kashiwakura T, Takahashi M, Suda Y (1995) Photoemission study of the spectral function of V_2O_3 in relation to the recent quantum Monte Carlo study. J Phys Soc Jpn 64:1230–1235
176. Kenny N, Kannewurf CR, Whitmore DH (1966) Optical absorption coefficients of vanadium pentoxide single crystals. J Phys Chem Solids 27:1237–1246
177. Hong S, Kim E, Kim D-W, Sung T-H, No K (1997) On measurement of optical band gap of chromium oxide films containing both amorphous and crystalline phases. J Non-Cryst Solids 221:245–254
178. Xu HY, Xu SL, Li XD, Wang H, Yan H (2006) Chemical bath deposition of hausmannite Mn_3O_4 thin films. Appl Surf Sci 252:4091–4096
179. Shinde VR, Mahadik SB, Gujar TP, Lokhande CD (2006) Supercapacitive cobalt oxide (Co_3O_4) thin films by spray pyrolysis. Appl Surf Sci 252:7487–7492
180. Ghijsen J, Tjeng LH, van Elp J, Eskes H, Westerink J, Sawatzky GA, Czyzyk MT (1988) Electronic structure of Cu_2O and CuO. Phys Rev B 38:11322–11330
181. Faleev SV, van Schilfgaarde M, Kotani T (2004) All-electron self-consistent GW approximation: application to Si, MnO, and NiO. Phys Rev Lett 93:126406 (4 pp)
182. Sakuma R, Miyake T, Aryasetiawan F (2008) First-principles study of correlation effects in VO_2. Phys Rev B 78:075106 (9 pp)

183. Sakuma R, Miyake T, Aryasetiawan F (2009) Effective quasiparticle Hamiltonian based on Löwdin's orthogonalization. Phys Rev B 80:235128 (8 pp)
184. Punya A, Lambrecht WRL, van Schilfgaarde M (2011) Quasiparticle band structure of Zn-IV-N_2 compounds. Phys Rev B 84:165204 (10 pp)
185. Svane A, Christensen NE, Gorczyca I, van Schilfgaarde M, Chantis AN, Kotani T (2010) Quasiparticle self-consistent GW theory of III-V nitride semiconductors: bands, gap bowing, and effective masses. Phys Rev B 82:115102 (6 pp)
186. Vidal J, Trani F, Bruneval F, Marques MAL, Botti S (2010) Effects of electronic and lattice polarization on the band structure of delafossite transparent conductive oxides. Phys Rev Lett 104:136401 (4 pp)
187. Botti S, Marques MAL (2013) Strong renormalization of the electronic band gap due to lattice polarization in the GW formalism. Phys Rev Lett 110:226404 (5 pp)
188. Friedrich C, Müller MC, Blügel S (2011) Band convergence and linearization error correction of all-electron GW calculations: the extreme case of zinc oxide. Phys Rev B 83:081101 (4 pp)
189. Salpeter EE, Bethe HA (1951) A relativistic equation for bound-state problems. Phys Rev 84:1232–1242
190. Nakanishi N (1969) A general survey of the theory of the Bethe-Salpeter equation. Prog Theor Phys Suppl 43:1–81
191. Rödl C, Bechstedt F (2012) Optical and energy-loss spectra of the antiferromagnetic transition metal oxides MnO, FeO, CoO, and NiO including quasiparticle and excitonic effects. Phys Rev B 86:235122 (11 pp)
192. Schleife A, Rödl C, Fuchs F, Furthmüller J, Bechstedt F (2009) Optical and energy-loss spectra of MgO, ZnO, and CdO from ab initio many-body calculations. Phys Rev B 80: 035112 (10 pp)
193. Reining L, Olevano V, Rubio A, Onida G (2002) Excitonic effects in solids described by time-dependent density-functional theory. Phys Rev Lett 88:066404 (4 pp)
194. Adragna G, Del Sole R, Marini A (2003) Ab initio calculation of the exchange-correlation kernel in extended systems. Phys Rev B 68:165108 (5 pp)
195. Bruneval F, Sottile F, Olevano V, Del Sole R, Reining L (2005) Many-body perturbation theory using the density-functional concept: beyond the GW approximation. Phys Rev Lett 94:186402 (4 pp)
196. Shishkin M, Marsman M, Kresse G (2007) Accurate quasiparticle spectra from self-consistent GW calculations with vertex corrections. Phys Rev Lett 99:246403 (4 pp)
197. Srikant V, Clarke DR (1998) On the optical band gap of zinc oxide. J Appl Phys 83: 5447–5451
198. Hartree DR (1928) The wave mechanics of an atom with a non-Coulomb central field. Proc Camb Philos Soc 24:89–110
199. Fock V (1930) Näherungsmethode zur Lösung des quantenmechanischen Mehrkörper-problems. Z Für Phys 61:126–148
200. Strout DL, Scuseria GE (1995) A quantitative study of the scaling properties of the Hartree–Fock method. J Chem Phys 102:8448–8452
201. Ordejón P, Drabold DA, Grumbach MP, Martin RM (1993) Unconstrained minimization approach for electronic computations that scales linearly with system size. Phys Rev B 48: 14646–14649
202. Mauri F, Galli G, Car R (1993) Orbital formulation for electronic-structure calculations with linear system-size scaling. Phys Rev B 47:9973–9976
203. Li X-P, Nunes RW, Vanderbilt D (1993) Density-matrix electronic-structure method with linear system-size scaling. Phys Rev B 47:10891–10894
204. Chen X, Langlois J-M, Goddard WA (1995) Dual-space approach for density-functional calculations of two- and three-dimensional crystals using Gaussian basis functions. Phys Rev B 52:2348–2361
205. Hernández E, Gillan MJ (1995) Self-consistent first-principles technique with linear scaling. Phys Rev B 51:10157–10160

206. Hernández E, Gillan MJ, Goringe CM (1996) Linear-scaling density-functional-theory technique: the density-matrix approach. Phys Rev B 53:7147–7157
207. White CA, Johnson BG, Gill PMW, Head-Gordon M (1994) The continuous fast multipole method. Chem Phys Lett 230:8–16
208. Kutteh R, Nicholas JB (1995) Efficient dipole iteration in polarizable charged systems using the cell multipole method and application to polarizable water. Comput Phys Commun 86: 227–235
209. Challacombe M, Schwegler E, Almlöf J (1996) Fast assembly of the Coulomb matrix: a quantum chemical tree code. J Chem Phys 104:4685–4698
210. Schwegler E, Challacombe M (1996) Linear scaling computation of the Hartree–Fock exchange matrix. J Chem Phys 105:2726–2734
211. Pople JA, Binkley JS, Seeger R (1976) Theoretical models incorporating electron correlation. Int J Quantum Chem 10:1–19
212. Schütz M, Hetzer G, Werner H-J (1999) Low-order scaling local electron correlation methods. I. Linear scaling local MP2. J Chem Phys 111:5691–5705
213. Ayala PY, Scuseria GE (1999) Linear scaling second-order Moller–Plesset theory in the atomic orbital basis for large molecular systems. J Chem Phys 110:3660–3671
214. Hetzer G, Schütz M, Stoll H, Werner H-J (2000) Low-order scaling local correlation methods II: splitting the Coulomb operator in linear scaling local second-order Møller–Plesset perturbation theory. J Chem Phys 113:9443–9455
215. Werner H-J, Manby FR, Knowles PJ (2003) Fast linear scaling second-order Møller-Plesset perturbation theory (MP2) using local and density fitting approximations. J Chem Phys 118:8149–8160
216. Doser B, Lambrecht DS, Ochsenfeld C (2008) Tighter multipole-based integral estimates and parallel implementation of linear-scaling AO–MP2 theory. Phys Chem Chem Phys 10: 3335–3344
217. Roos BO, Taylor PR, Siegbahn PEM (1980) A complete active space SCF method (CASSCF) using a density matrix formulated super-CI approach. Chem Phys 48:157–173
218. Veryazov V, Malmqvist PÅ, Roos BO (2011) How to select active space for multiconfigurational quantum chemistry? Int J Quantum Chem 111:3329–3338
219. Andersson K, Malmqvist PÅ, Roos BO, Sadlej AJ, Wolinski K (1990) Second-order perturbation theory with a CASSCF reference function. J Phys Chem 94:5483–5488
220. Shavitt I (1998) The history and evolution of configuration interaction. Mol Phys 94:3–17
221. Dreuw A, Head-Gordon M (2005) Single-reference ab initio methods for the calculation of excited states of large molecules. Chem Rev 105:4009–4037
222. Chwee TS, Szilva AB, Lindh R, Carter EA (2008) Linear scaling multireference singles and doubles configuration interaction. J Chem Phys 128:224106 (9 pp)
223. Chwee TS, Carter EA (2010) Cholesky decomposition within local multireference singles and doubles configuration interaction. J Chem Phys 132:074104 (10 pp)
224. Chwee TS, Carter EA (2011) Valence excited states in large molecules via local multireference singles and doubles configuration interaction. J Chem Theory Comput 7: 103–111
225. Čížek J (1966) On the correlation problem in atomic and molecular systems. Calculation of wavefunction components in Ursell-type expansion using quantum-field theoretical methods. J Chem Phys 45:4256–4266
226. Stanton JF, Bartlett RJ (1993) The equation of motion coupled-cluster method. A systematic biorthogonal approach to molecular excitation energies, transition probabilities, and excited state properties. J Chem Phys 98:7029–7039
227. Sun J-Q, Bartlett RJ (1996) Second-order many-body perturbation-theory calculations in extended systems. J Chem Phys 104:8553–8565
228. Sun J-Q, Bartlett RJ (1996) Correlated prediction of the photoelectron spectrum of polyethylene: explanation of XPS and UPS measurements. Phys Rev Lett 77:3669–3672

229. Sun J-Q, Bartlett RJ (1997) Many-body perturbation theory for quasiparticle energies. J Chem Phys 107:5058–5071
230. Sun J-Q, Bartlett RJ (1998) Convergence behavior of many-body perturbation theory with lattice summations in polymers. Phys Rev Lett 80:349–352
231. Hirata S, Grabowski I, Tobita M, Bartlett RJ (2001) Highly accurate treatment of electron correlation in polymers: coupled-cluster and many-body perturbation theories. Chem Phys Lett 345:475–480
232. Pisani C, Maschio L, Casassa S, Halo M, Schütz M, Usvyat D (2008) Periodic local MP2 method for the study of electronic correlation in crystals: theory and preliminary applications. J Comput Chem 29:2113–2124
233. Marsman M, Grüneis A, Paier J, Kresse G (2009) Second-order Møller–Plesset perturbation theory applied to extended systems. I. Within the projector-augmented-wave formalism using a plane wave basis set. J Chem Phys 130:184103 (10 pp)
234. Grüneis A, Marsman M, Kresse G (2010) Second-order Møller–Plesset perturbation theory applied to extended systems. II. Structural and energetic properties. J Chem Phys 133:074107 (11 pp)
235. Shepherd JJ, Grüneis A, Booth GH, Kresse G, Alavi A (2012) Convergence of many-body wave-function expansions using a plane-wave basis: from homogeneous electron gas to solid state systems. Phys Rev B 86:035111 (14 pp)
236. Hirata S, Podeszwa R, Tobita M, Bartlett RJ (2004) Coupled-cluster singles and doubles for extended systems. J Chem Phys 120:2581–2592
237. Evjen HM (1932) On the stability of certain heteropolar crystals. Phys Rev 39:675–687
238. Burow AM, Sierka M, Döbler J, Sauer J (2009) Point defects in CaF_2 and CeO_2 investigated by the periodic electrostatic embedded cluster method. J Chem Phys 130:174710 (11 pp)
239. Dungsrikaew V, Limtrakul J, Hermansson K, Probst M (2004) Comparison of methods for point-charge representation of electrostatic fields. Int J Quantum Chem 96:17–22
240. Sousa C, Casanovas J, Rubio J, Illas F (1993) Madelung fields from optimized point charges for ab initio cluster model calculations on ionic systems. J Comput Chem 14:680–684
241. Mulliken RS (1955) Electronic population analysis on LCAO-MO molecular wave functions. I. J Chem Phys 23:1833–1840
242. Löwdin P-O (1970) On the nonorthogonality problem. In: Löwdin P-O (ed) Adv Quantum Chem. Academic, New York, pp 185–199
243. Hirshfeld FL (1977) Bonded-atom fragments for describing molecular charge densities. Theor Chim Acta 44:129–138
244. Bader RF (1994) Atoms in molecules: a quantum theory. Clarendon, Oxford
245. Henkelman G, Arnaldsson A, Jónsson H (2006) A fast and robust algorithm for Bader decomposition of charge density. Comput Mater Sci 36:354–360
246. Sanville E, Kenny SD, Smith R, Henkelman G (2007) Improved grid-based algorithm for Bader charge allocation. J Comput Chem 28:899–908
247. Tang W, Sanville E, Henkelman G (2009) A grid-based Bader analysis algorithm without lattice bias. J Phys Condens Matter 21:084204 (7 pp)
248. Casarin M, Maccato C, Vittadini A (1998) Molecular chemisorption on TiO_2(110): a local point of view. J Phys Chem B 102:10745–10752
249. Kadossov EB, Gaskell KJ, Langell MA (2007) Effect of surrounding point charges on the density functional calculations of Ni_xO_x clusters ($x = 4-12$). J Comput Chem 28:1240–1251
250. Neyman KM, Rösch N (1992) CO bonding and vibrational modes on a perfect MgO(001) surface: LCGTO-LDF model cluster investigation. Chem Phys 168:267–280
251. Yudanov IV, Nasluzov VA, Neyman KM, Rösch N (1997) Density functional cluster description of ionic materials: improved boundary conditions for MgO clusters with the help of cation model potentials. Int J Quantum Chem 65:975–986
252. Winter NW, Pitzer RM, Temple DK (1987) Theoretical study of a Cu^+ ion impurity in a NaF host. J Chem Phys 86:3549–3556

253. Kanan DK, Sharifzadeh S, Carter EA (2012) Quantum mechanical modeling of electronic excitations in metal oxides: magnesia as a prototype. Chem Phys Lett 519–520:18–24
254. Barandiarán Z, Seijo L (1988) The ab initio model potential representation of the crystalline environment. Theoretical study of the local distortion on NaCl:Cu^+. J Chem Phys 89: 5739–5746
255. Pascual JL, Barros N, Barandiarán Z, Seijo L (2009) Improved embedding ab initio model potentials for embedded cluster calculations. J Phys Chem A 113:12454–12460
256. Shluger AL, Gale JD (1996) One-center trapping of the holes in alkali halide crystals. Phys Rev B 54:962–969
257. Sushko PV, Shluger AL, Catlow CRA (2000) Relative energies of surface and defect states: ab initio calculations for the MgO (001) surface. Surf Sci 450:153–170
258. Nasluzov VA, Rivanenkov VV, Gordienko AB, Neyman KM, Birkenheuer U, Rösch N (2001) Cluster embedding in an elastic polarizable environment: density functional study of Pd atoms adsorbed at oxygen vacancies of MgO(001). J Chem Phys 115:8157–8171
259. De Graaf C, Broer R, Nieuwpoort WC (1996) Electron correlation effects on the d-d excitations in NiO. Chem Phys 208:35–43
260. Domingo A, Rodríguez-Fortea A, Swart M, de Graaf C, Broer R (2012) Ab initio absorption spectrum of NiO combining molecular dynamics with the embedded cluster approach in a discrete reaction field. Phys Rev B 85:155143 (15 pp)
261. De Vries AH, Van Duijnen PT, Juffer AH, Rullmann JAC, Dijkman JP, Merenga H, Thole BT (1995) Implementation of reaction field methods in quantum chemistry computer codes. J Comput Chem 16:37–55
262. Liao P, Carter EA (2011) Optical excitations in Hematite (α-Fe_2O_3) via embedded cluster models: a CASPT2 study. J Phys Chem C 115:20795–20805
263. Merchant P, Collins R, Kershaw R, Dwight K, Wold A (1979) The electrical, optical and photoconducting properties of $Fe_{2-x}Cr_xO_3$ ($0 \leq x \geq 0.47$). J Solid State Chem 27:307–315
264. De Graaf C, Broer R (2000) Midinfrared spectrum of undoped cuprates: d-d transitions studied by ab initio methods. Phys Rev B 62:702–709
265. Kanan DK, Carter EA (2013) Optical excitations in MnO and MnO:ZnO via embedded CASPT2 theory and their implications for solar energy conversion. J Phys Chem C 117: 13816–13826
266. Muñoz-García AB, Seijo L (2010) Structural, electronic, and spectroscopic effects of Ga codoping on Ce-doped yttrium aluminum garnet: first-principles study. Phys Rev B 82: 184118 (10 pp)
267. Muñoz-García AB, Pascual JL, Barandiarán Z, Seijo L (2010) Structural effects and 4f-5d transition shifts induced by La codoping in Ce-doped yttrium aluminum garnet: first-principles study. Phys Rev B 82:064114 (8 pp)
268. Geleijns M, de Graaf C, Broer R, Nieuwpoort WC (1999) Theoretical study of local electronic transitions in the NiO(100) surface. Surf Sci 421:106–115
269. Fink K (2005) Ab initio cluster calculations for the absorption energies of F and F^+ centers in bulk ZnO. Phys Chem Chem Phys 7:2999–3004
270. Fink R, Staemmler V (1993) A multi-configuration reference CEPA method based on pair natural orbitals. Theor Chim Acta 87:129–145
271. Hozoi L, de Vries AH, Broer R, de Graaf C, Bagus PS (2006) Ni 3s-hole states in NiO by non-orthogonal configuration interaction. Chem Phys 331:178–185
272. Bagus PS, Ilton ES (2006) Effects of covalency on the p-shell photoemission of transition metals: MnO. Phys Rev B 73:155110 (14 pp)
273. Grimley TB, Pisani C (1974) Chemisorption theory in the Hartree-Fock approximation. J Phys C Solid State Phys 7:2831–2848
274. Gunnarsson O, Hjelmberg H (1975) Hydrogen chemisorption by the spin-density functional formalism. I. Phys Scr 11:97–103
275. Gunnarsson O, Hjelmberg H, Lundqvist BI (1977) Calculation of geometries and chemisorption energies of adatoms on simple metals. Surf Sci 63:348–357

276. Pisani C (1978) Approach to the embedding problem in chemisorption in a self-consistent-field-molecular-orbital formalism. Phys Rev B 17:3143–3153
277. Pisani C, Dovesi R, Carosso P (1979) Moderately-large-embedded-cluster approach to the study of local defects in solids. Vacancy and substitutional impurities in graphite. Phys Rev B 20:5345–5357
278. Pisani C, Dovesi R, Ugliengo P (1983) Comparison of different approaches to the study of local defects in crystals. I. Theoretical considerations and computational schemes. Phys Stat Sol B 116:249–259
279. Pisani C, Dovesi R, Nada R, Kantorovich LN (1990) Ab initio Hartree–Fock perturbed-cluster treatment of local defects in crystals. J Chem Phys 92:7448–7460
280. Inglesfield JE (2001) Embedding at surfaces. Comput Phys Commun 137:89–107
281. Scheffler M, Droste C, Fleszar A, Máca F, Wachutka G, Barzel G (1991) A self-consistent surface-Green-function (SSGF) method. Phys B Condens Matter 172:143–153
282. Whitten JL, Pakkanen TA (1980) Chemisorption theory for metallic surfaces: electron localization and the description of surface interactions. Phys Rev B 21:4357–4367
283. Whitten JL (1981) Chemisorption theory for metallic surfaces: convergence of surface localized orbitals for Ti(0001) clusters. Phys Rev B 24:1810–1817
284. Whitten JL (1993) Theoretical studies of surface reactions: embedded cluster theory. Chem Phys 177:387–397
285. Danyliv O, Kantorovich L (2004) Comparison of localization procedures for applications in crystal embedding. Phys Rev B 70:075113 (12 pp)
286. McWeeny R (1960) Some recent advances in density matrix theory. Rev Mod Phys 32: 335–369
287. Huzinaga S, Cantu AA (1971) Theory of separability of many-electron systems. J Chem Phys 55:5543–5549
288. Birkenheuer U, Fulde P, Stoll H (2006) A simplified method for the computation of correlation effects on the band structure of semiconductors. Theor Chem Accounts 116:398–403
289. Hozoi L, Birkenheuer U, Fulde P, Mitrushchenkov A, Stoll H (2007) Ab initio wave function-based methods for excited states in solids: correlation corrections to the band structure of ionic oxides. Phys Rev B 76:085109 (10 pp)
290. Cortona P (1991) Self-consistently determined properties of solids without band-structure calculations. Phys Rev B 44:8454–8458
291. Wesolowski TA, Warshel A (1993) Frozen density functional approach for ab initio calculations of solvated molecules. J Phys Chem 97:8050–8053
292. Govind N, Wang YA, da Silva AJR, Carter EA (1998) Accurate ab initio energetics of extended systems via explicit correlation embedded in a density functional environment. Chem Phys Lett 295:129–134
293. Govind N, Wang YA, Carter EA (1999) Electronic-structure calculations by first-principles density-based embedding of explicitly correlated systems. J Chem Phys 110:7677–7688
294. Klüner T, Govind N, Wang YA, Carter EA (2001) Prediction of electronic excited states of adsorbates on metal surfaces from first principles. Phys Rev Lett 86:5954–5957
295. Klüner T, Govind N, Wang YA, Carter EA (2002) Periodic density functional embedding theory for complete active space self-consistent field and configuration interaction calculations: ground and excited states. J Chem Phys 116:42–54
296. Klüner T, Govind N, Wang YA, Carter EA (2002) Klüner et al. reply. Phys Rev Lett 88: 209702
297. Huang P, Carter EA (2006) Self-consistent embedding theory for locally correlated configuration interaction wave functions in condensed matter. J Chem Phys 125:084102 (14 pp)
298. Sharifzadeh S, Huang P, Carter EA (2009) All-electron embedded correlated wavefunction theory for condensed matter electronic structure. Chem Phys Lett 470:347–352
299. Thomas LH (1927) The calculation of atomic fields. Math Proc Camb Philos Soc 23:542–548

300. Fermi E (1928) Eine statistische Methode zur Bestimmung einiger Eigenschaften des Atoms und ihre Anwendung auf die Theorie des periodischen Systems der Elemente. Z Für Phys 48:73–79
301. Von Weizsäcker CF (1935) Zur Theorie der Kernmassen. Z Für Phys 96:431–458
302. Wang L-W, Teter MP (1992) Kinetic-energy functional of the electron density. Phys Rev B 45:13196–13220
303. Wang YA, Govind N, Carter EA (1998) Orbital-free kinetic-energy functionals for the nearly free electron gas. Phys Rev B 58:13465–13471
304. Wang YA, Govind N, Carter EA (1999) Orbital-free kinetic-energy density functionals with a density-dependent kernel. Phys Rev B 60:16350–16358
305. Goodpaster JD, Ananth N, Manby FR, Miller TF (2010) Exact nonadditive kinetic potentials for embedded density functional theory. J Chem Phys 133:084103–084110
306. Goodpaster JD, Barnes TA, Miller TF (2011) Embedded density functional theory for covalently bonded and strongly interacting subsystems. J Chem Phys 134:164108–164109
307. Levy M (1979) Universal variational functionals of electron densities, first-order density matrices, and natural spin-orbitals and solution of the v-representability problem. Proc Natl Acad Sci 76:6062–6065
308. Zhao Q, Parr RG (1992) Quantities $T_s[n]$ and $T_c[n]$ in density-functional theory. Phys Rev 46: 2337–2343
309. Zhao Q, Parr RG (1993) Constrained-search method to determine electronic wave functions from electronic densities. J Chem Phys 98:543–548
310. Zhao Q, Morrison RC, Parr RG (1994) From electron densities to Kohn-Sham kinetic energies, orbital energies, exchange-correlation potentials, and exchange-correlation energies. Phys Rev 50:2138–2142
311. King RA, Handy NC (2000) Kinetic energy functionals from the Kohn–Sham potential. Phys Chem Chem Phys 2:5049–5056
312. Fux S, Jacob CR, Neugebauer J, Visscher L, Reiher M (2010) Accurate frozen-density embedding potentials as a first step towards a subsystem description of covalent bonds. J Chem Phys 132:164101 (18 pp)
313. Wu Q, Yang W (2003) A direct optimization method for calculating density functionals and exchange–correlation potentials from electron densities. J Chem Phys 118:2498–2509
314. Roncero O, de Lara-Castells MP, Villarreal P, Flores F, Ortega J, Paniagua M, Aguado A (2008) An inversion technique for the calculation of embedding potentials. J Chem Phys 129: 184104 (12 pp)
315. Roncero O, Zanchet A, Villarreal P, Aguado A (2009) A density-division embedding potential inversion technique. J Chem Phys 131:234110 (7 pp)
316. Huang C, Pavone M, Carter EA (2011) Quantum mechanical embedding theory based on a unique embedding potential. J Chem Phys 134:154110 (11 pp)
317. Cohen MH, Wasserman A (2003) Revisiting N-continuous density-functional theory: chemical reactivity and "atoms" in "molecules". Isr J Chem 43:219–227
318. Cohen MH, Wasserman A (2006) On hardness and electronegativity equalization in chemical reactivity theory. J Stat Phys 125:1121–1139
319. Cohen MH, Wasserman A (2007) On the foundations of chemical reactivity theory. J Phys Chem A 111:2229–2242
320. Elliott P, Cohen MH, Wasserman A, Burke K (2009) Density functional partition theory with fractional occupations. J Chem Theory Comput 5:827–833
321. Elliott P, Burke K, Cohen MH, Wasserman A (2010) Partition density-functional theory. Phys Rev 82:024501 (4 pp)
322. Huang C, Carter EA (2011) Potential-functional embedding theory for molecules and materials. J Chem Phys 135:194104 (17 pp)
323. Manby FR, Stella M, Goodpaster JD, Miller TF (2012) A simple, exact density-functional-theory embedding scheme. J Chem Theory Comput 8:2564–2568

324. Nafziger J, Wu Q, Wasserman A (2011) Molecular binding energies from partition density functional theory. J Chem Phys 135:234101 (6 pp)
325. Huang P, Carter EA (2006) Local electronic structure around a single Kondo impurity. Nano Lett 6:1146–1150
326. Huang P, Carter EA (2008) Ab initio explanation of tunneling line shapes for the Kondo impurity state. Nano Lett 8:1265–1269
327. Sharifzadeh S, Huang P, Carter EA (2009) Origin of tunneling lineshape trends for Kondo states of Co adatoms on coinage metal surfaces. J Phys Condens Matter 21:355501 (8 pp)
328. Libisch F, Huang C, Liao P, Pavone M, Carter EA (2012) Origin of the energy barrier to chemical reactions of O_2 on Al(111): evidence for charge transfer, not spin selection. Phys Rev Lett 109:198303 (5 pp)
329. Mukherjee S, Libisch F, Large N, Neumann O, Brown LV, Cheng J, Lassiter JB, Carter EA, Nordlander P, Halas NJ (2013) Hot electrons do the impossible: plasmon-induced dissociation of H_2 on Au. Nano Lett 13:240–247
330. Roessler DM, Walker WC (1967) Electronic spectrum and ultraviolet optical properties of crystalline MgO. Phys Rev 159:733–738
331. Bortz ML, French RH, Jones DJ, Kasowski RV, Ohuchi FS (1990) Temperature dependence of the electronic structure of oxides: MgO, $MgAl_2O_4$ and Al_2O_3. Phys Scr 41:537–541
332. Benedict LX, Shirley EL, Bohn RB (1998) Optical absorption of insulators and the electron–hole interaction: an ab initio calculation. Phys Rev Lett 80:4514–4517
333. Wang N-P, Rohlfing M, Krüger P, Pollmann J (2004) Electronic excitations of CO adsorbed on MgO(001). Appl Phys 78:213–221
334. Hozoi L, Siurakshina L, Fulde P, van den Brink J (2011) Ab initio determination of Cu 3d orbital energies in layered copper oxides. Sci Rep 1:65. doi:10.1038/srep00065